UCRL--93584

DE86 003491

[illegible]

Atomic Vapor Laser Isotope Separation

R.C. Stern
J.A. Paisner

This paper was prepared for submittal to:
First International Laser Science Conference
Dallas, TX
November 18–22, 1985

November 8, 1985

Lawrence
Livermore
National
Laboratory

ATOMIC VAPOR LASER ISOTOPE SEPARATION*

ABSTRACT

Atomic vapor laser isotope separation (AVLIS) is a general and powerful technique. A major present application to the enrichment of uranium for light-water power reactor fuel has been under development for over 10 years. In June 1985 the Department of Energy announced the selection of AVLIS as the technology to meet the nation's future need for the internationally competitive production of uranium separative work. The economic basis for this decision is considered, with an indication of the constraints placed on the process figures of merit and the process laser system. We then trace an atom through a generic AVLIS separator and give examples of the physical steps encountered, the models used to describe the process physics, the fundamental parameters involved, and the role of diagnostic laser measurements.

Atomic vapor laser isotope separation (AVLIS) is a general process for converting a feed stream into a product stream in which a selected set of isotopes has been enriched or depleted. The heart of the process is the selective multistep photoionization of an atomic vapor stream. The components of a generic AVLIS process are shown in Fig. 1. The process hardware is divided into a separator system and a laser system that are, to a great degree, mechanically independent. Atomic vapor is produced in the vaporizer and expands upwards in vacuum. Tunable laser frequencies are generated in a dye laser system that is in turn driven by a pump laser system. Copper-vapor lasers serve as the pump lasers in the major systems we have constructed to date. Both the pump lasers and tunable lasers are configured in master-oscillator/power-amplifier (MOPA) chains. The laser light illuminates the atomic vapor between the plates of an ion extractor. Photoions are drawn to and neutralized at negatively biased extractor plates. The remaining vapor streams through to the roof of the separator. In an enrichment mission the material from the extractor is enriched product; the material from the roof is

---

Work performed under the auspices of the US Department of Energy by the Lawrence Livermore National Laboratory under Contract W-7405-Eng-48.

depleted tails. In a stripping mission, product and tails are reversed. At Livermore, we have investigated the application of this laser isotope separation technology to a number of missions, some of which are shown in Fig. 2. The dominant mission is clearly the enrichment of uranium for use in civilial light-water reactors.

When the Livermore program began in 1973, there were many isotope separation concepts extant in the community. For uranium isotopes, laser photodissociation of uranium hexafluoride (UF_6) and photoionization of atomic uranium (U) vapor were receiving the greatest financial support. A molecular UF_6 process was being developed primarily by Los Alamos and an atomic process was being developed primarily by JNAI, Inc., a joint venture between Exxon Nuclear and AVCO. A large number of scientific concepts based on atoms, molecules, and molecular fragments in gaseous, liquid, and solid phases were evaluated by Livermore, both theoretically and experimentally, before our choice of AVLIS as the process with the greatest technological and economic promise. Laser isotope separation technology for uranium enrichment has been under development at Livermore since 1973 in a joint effort with Oak Ridge.

In June 1985, following an intensive year-long review, the Department of Energy selected AVLIS as the technology to meet the nation's future need for competitive production of enriched uranium. The selection is an opportunity and a challenge for the AVLIS program and, indirectly, for the laser community as a whole. We have been invited to bring to commercial scale a process that uses lasers as more than focusable candles.

Some of the background for this decision can be understood by looking at the projected market for uranium enrichment, as shown in Fig. 3. Uranium enrichment is sold in separative work units, or SWUs, which will be defined below. Of the total market in the 1990s, well under half is domestic. An increasing fraction of the market is expected to be competitive. Utilities will purchase enrichment in a world-wide market where they can find the lowest prices.

The result will be a downward trend in the price for SWUs, as projected in Fig 4. This trend is driven by a growing uranium enrichment capacity and by the introduction in Europe of new enrichment technology. For the US to remain competitive, we must have an enrichment technology in hand that can operate at these lower prices. The competitive market in the year 2000 is expected to be roughly $1 billion/y, larger than the total domestic market.

We can see what these enrichment prices imply by examining the SWU (Fig. 5). The SWU is a value function, with units of mass, which depends on the mass flows and assays. The expression comes from cascade theory. It is related to, but not proportional to, the entropy of mixing destroyed by the enrichment process. To make this clearer, for natural uranium feed, light-water-reactor fuel product, and typical tails assay, 1 SWU converts 1.24 kg of feed into 0.21 kg of product. In other words, the world demand corresponds to processing 40,000 Mg of uranium feed/year. Hence any uranium-enrichment process involves large-scale hardware.

Setting a target at the low end of the range of projected prices, we want a future enrichment process such as AVLIS to come in at less than $60/SWU. This corresponds to a process cost of less than $49/kg of feed or less than $286/kg of product. Breaking the SWU cost into components as shown in Fig. 6, we find two components that reflect the process engineering costs for the materials-handling and laser systems and two components that reflect the process physics; i.e., the laser energy required to process one unit of feed and the separative work obtained from that feed.

To evaluate what is required of the laser system, we can estimate the megajoules of laser energy required to process 1 kg of feed (Fig. 7). Outside of conversion factors, the laser energy is the product of the photon utilization (i.e., the fraction of the required photons that is actually absorbed--accounting for the saturation level necessary to drive the laser/atom kinetics and the light losses in optical elements), the absorbed photon energy needed to process one atom (about 6 eV for any typical photoionization or photodissociation process), and the fraction of the atoms that absorbs the light. For a process such as uranium enrichment, where the isotope of interest is only a very small fraction of the vapor (0.0072 mole fraction), it is essential to have very high photoselectivity. Otherwise absorption in unwanted isotopes will dominate and require a larger laser system.

Putting in values characteristic of the AVLIS process, including the very high process photoselectivity, roughly 100 kJ of laser energy are needed to process 1 kg of uranium feed. Using typical costs for an engineered laser system, we expect the laser cost/kg of feed to be on the order of $10.

The other half of the physics performance is the separative work generated per kg of feed. Figure 8, which is a map of separative work performance vs product and tails assays, shows that high SWU production corresponds to low tails assays, not to high product assays, as one might naively think. The goal for the physics of the AVLIS process is therefore clear. We want a process that strips a very high fraction of the ^{235}U atoms out of the feed, leaving few ^{235}U in the tails. All of our modeling and experiments to date indicate that we can obtain a high stripping efficiency and that the DOE target prices can be met with the AVLIS process.

With this background we can turn to the physics of the process and examine in more detail the physical steps an atom encounters as it passes through an AVLIS separator (Fig. 9). Uranium vapor is generated by an electron beam striking uranium metal held in a cooled crucible. This type of vaporization is commonly used in the metal-plating industry. What is unusual about our application is that uranium is highly refractory (the metal boils at 4100 K) and that very high vaporization rates are desired. The vapor then undergoes adiabatic free expansion into vacuum, in the course of which it transits all of the regimes of aerodynamics: continuum flow near the source, transition flow as the vapor expands, and eventually free molecular flow. The resulting vapor flow is cooled and is hypersonic.

As the vapor passes between the extractor plates, it is illuminated by three superimposed laser pulses of the frequencies necessary to drive a three-step photoionization. The initial photoplasma contains, to a very good approximation, only ^{235}U ions. If the plasma were left unperturbed, resonant charge exchange between ^{235}U ions and ^{238}U neutrals would in time restore the ion population to natural abundance. This sets a time scale we must meet in the extraction process. Therefore the photoplasma is rapidly extracted; the ions going to negatively biased extractor plates, the electrons going to positively biased surfaces or to ground.

Finally, the enriched product is collected from the plates and the depleted tails are collected from the roof. In order to obtain the economic advantages of continuous operation, the streams are collected by liquid flow. This obviously means that the collecting surfaces run at high temperature. We are in a sense doing precision laser physics inside a foundry.

There is more physics involved here than one can cover in a single talk. Therefore we have chosen to focus on three specific aspects of the process: the dynamics of the liquid-metal pool in the vaporizer, the laser diagnostic measurements of vapor properties, and the laser measurements of the spectroscopic parameters that enter the photoionization process. In each area we will describe some of the physics models we use and some of the experimental information we collect to validate these models.

The phenomena involved in uranium vaporization are indicated in Fig. 10. Uranium in a cooled crucible is heated by a primary electron beam impinging from above. From the point of view of the rest of the separator, the vaporizer appears as a source of vapor, secondary electrons, and thermal radiation, all of which must be accounted for in the design. The liquid pool, whose temperatures determine the vaporization rate, is bounded by two surfaces whose positions are not fixed inputs, but are determined by the dynamics of the problem: the lower solid/liquid interface and the upper trench produced by the thrust of the departing vapor.

The objective of vaporizer design is to maximize the mass vaporized per input electron-beam power. This is equivalent to maximizing the temperature rise from the crucible to the vaporizing hot zone under the electron beam. What we observe experimentally is a classic instability in systems that are strongly heated from above. The entire liquid pool is set into bulk convective motion. This convection short circuits the crucible-to-hot-zone temperature rise, reducing source efficiency.

When we set out to model the behavior of the liquid pool, with the aim of prediction and eventually control, we found that we engaged a remarkably complex physical situation (Fig. 11). Given a pool velocity and temperature field, we can evaluate the buoyancy, surface tension, and vapor-thrust forces and predict a free surface profile. Likewise, given the heat transported to the liquid/solid interface by the pool, we can evaluate the thermal transport through the solid skull to the crucible and see if the heat fluxes match at the chosen interface position. With the boundaries set, we perform a transient solution of the appropriate fluid mechanical equations in two dimensions, using a powerful finite-element technique, to obtain the velocity and temperature field in the liquid pool and the resulting vaporization rate and efficiency. Iteration to self-consistency on the boundary conditions is a major undertaking that is at the limit of our computational resources.

The flow patterns are not simple. We found not only the expected major circulation up under the hot zone and down to the lower boundary, but also detached vortices under the hot zone, which influence the vaporization temperatures.

We also found that the flow, while laminar, is chaotic due to time variation in the eddy structure, so that the properties such as surface temperature do not come to a steady state (Fig. 12). The model has been tested against a limited amount of experimental information. We cannot measure the liquid/solid interface location while the vaporizer is operating. However, we can find the interface location by examining the crystal morphology in post-run frozen sections of the melt. When this boundary is input, we calculate free surface velocities in qualitative agreement with those measured from video pictures of the operating melt and hot-zone temperatures in qualitative agreement with stagnation temperatures deduced from the total energy in the vapor after expansion. We are now developing better diagnostics and moving from qualitative to quantitative agreement in the model.

A major use of lasers in the program has been in the measurement of the properties of the vapor stream. A remarkable number of vapor properties have some bearing on the process design, as indicated in Fig. 13. The magnitude of the bulk flow velocity determines the laser pulse-repetition frequency (prf) required to illuminate the vapor. The direction of the bulk flow sets the geometric alignment of the extractor. The random-velocity components or temperature in the radial direction determines the prf necessary to illuminate the fastest atoms with the lasers. The transverse temperature gives the amount of material from the flow directly plated on the extractor. The axial temperature sets the Doppler line width of the laser transitions. The distribution of atoms among the atom's electronic states determines what fraction of the atomic population can be addressed by the photoionizing lasers. Finally, the overall density distribution in the flow at a particular standoff distance tells us the angular span we need to cover with the extractor.

The distinction that we make between the thermal-velocity distributions along and across the flow is a characteristic signature of the breakdown of local thermodynamic equilibrium in transition flow. These temperature splittings are a familiar feature of free expansions from a point source. They are not as familiar for the cylindrical flow from a line source into an angular wedge, which we encounter in the AVLIS process. Accordingly, we have used the Bird--Monte Carlo technique to model the transition flow in this geometry. As shown in Fig. 14, we start a high-density flow from an entrance surface just above the sonic line. The simulation develops the flow from a free-molecular field to the field with collisions, in a two-dimensional wedge of effectively infinite length, by following individual atomic trajectories.

A typical evolution of the flow, in this case for helium, is illustrated in Fig. 15 by the transverse (θ) velocity distributions, sampled on the azimuthal centerline. The distributions remain Maxwellian and cool from a Mach number of 2 to a Mach number of 6.5. The evolution of all three velocity components is shown in Fig. 16. The solid line is the continuum flow result, from a method of characteristics calculation. In a point-source expansion, the two transverse temperatures fall below the continuum line due to geometric cooling, while the radial component freezes out at a constant temperature. The pattern here is essentially different. Unlike a point-source expansion, expansion from a line source never runs out of collisions.

The diagnostic laser system we use to make measurements of the vapor properties is not unusual in any of its components. What we have done is automate and integrate the system so that it gives us simultaneous real-time information on a routine basis. The front end of the diagnostic laser system is shown schematically in Fig. 17. A commercial ring dye laser is coarsely tuned with a monochromator and discharge lamp, then centered on line using the opto-galvanic signal from a hollow cathode. The process-control computer system drives the laser frequency scan, logs the scan interferometrically, and monitors the hollow cathode to ensure the line remains captured in the scan.

The individually modulated scans at five frequencies are then combined into single-mode optical fibers and transported to the separator (Fig. 18). At the separator the output from each fiber is again split, characteristically into three beams, and sent to one of three types of probes. Up to 12 demodulated signal and reference voltages are sent in parallel to the computer.

A layout of the simplest probe, an axial absorption shot down the length of the separator, is shown in Fig. 19. We can arrange these probes to track the evolution of the vapor along a flow streamline as a function of standoff distance from the source. Figure 20 shows an array of 2-axis point probes before installation. The supporting structure carries the two input and two output optical fibers to each probe, as well as the water cooling necessary to preserve the probes in an enclosure running above the melting point of uranium.

The process-control computer captures the signal, reference, and interferometer scans, linearizes the frequency scale, and determines the absorption (Fig. 21). Absolute densities in individual electronic states are determined using vapor path lengths and optical cross sections stored in a relational data base. Line shapes are fit to determine velocity distributions, temperatures, and Mach numbers. Time histories and cross plots are available on demand on control-room consoles. The time from ordering a scan to updating the display is under 10 s. Figure 22 is a typical display showing time histories of neutral and ion densities. Relative coordinates were inserted for this picture; in practice the displays are absolute.

As a sample of the large amount of information we have obtained with these laser diagnostics, Fig. 23 is a cross plot of uranium bulk flow velocity vs neutral density at one point in a series of experiments where the vaporizer geometry was varied. One sees the approach to terminal velocity typical of a free expansion. Figure 24 is a published example of electronic state populations, here in Nd, showing the electronic cooling that takes place in the expansion.

The flow chart in Fig. 25 illustrates the detailed analysis and experimental data base we employ in photoionization physics. Our theoretical approach includes a first-principles model based on integrating Schrodinger's equation. This computer model, named SHUX, uses as input a complete set of experimentally measured spectroscopic parameters corresponding to the relevant transitions of the atom of interest. The code treats the coherent multiple laser/atom interactions and accounts for the evolution of every magnetic sublevel and velocity class within each hyperfine level in the excitation sequence. The code also computes the atomic polarizations driven by the light fields and thus facilitates analysis of the back reaction of the atoms on the propagating lasers. Figure 26 shows an example of three-step photoionization of ^{157}Gd (nuclear spin I = 3/2) using simultaneous excitation by single-mode lasers tuned to the center of gravity of levels in a $J = 2 \rightarrow 2 \rightarrow 1 \rightarrow 0$ ladder. One of the novel features of the AVLIS process and laser system developed at Livermore is that we can specify and control by design the spectral content of the tunable dye lasers to optimize overall photoionization performance.

A typical experimental configuration used to acquire AVLIS spectroscopic data for elements of interest is shown schematically in Fig. 27. Of particular note are the narrow-band pulsed dye laser and atomic beam systems routinely used in our laboratories. Figure 28 shows the narrow-band laser that produces several millijoules of 4 to 6 ns time-bandwidth-limited pulses used in coherent excitation experiments discussed later. Figure 29 shows a portable atomic beam system with a clam-shell enclosure for quick and easy maintenance. A schematic of the basic components contained within the vacuum envelope is shown in Fig. 30. The system is very versatile and allows us to employ many techniques including quadrupole mass filtering, field ionization and collection, and fluorescence detection. In some cases the high-temperature resistively heated oven is replaced by a laser ablation source.

Perhaps the simplest measurements to make in this system are of radiative lifetimes using time-delayed photoionization. Data for atomic gadolinium are illustrated in Fig. 31. The hyperfine spectra of the odd isotopes of atomic gadolinium (natural = 0.2% ^{152}Gd, 2.15% ^{154}Gd, 14.73% ^{155}Gd, 20.47% ^{156}Gd, 15.68% ^{157}Gd, 24.87% ^{158}Gd, 21.90% ^{160}Gd), shown in Fig. 32 for the 215-cm^{-1} to 17,380-cm^{-1} transition, were obtained using a collimated atomic beam, cw dye laser excitation, and fluorescence detection. The magnetic dipole and electric quadrupole hyperfine parameters (A and B, respectively) derived from these data for the upper level are displayed for the ^{157}Gd isotope. The isotope shifts arising from nuclear volume effects are also indicated. Note that the ^{160}Gd and ^{152}Gd peaks are outside the range shown in this particular spectral scan. It is these splittings and shifts in the electronic transitions in heavy atoms that are exploited in the AVLIS process to attain high isotopic photoselectivity.

In situations where small hyperfine splittings and isotope shifts are encountered, such as that illustrated for the odd isotopes of gadolinium in Fig. 32, polarization selection rules can be used to achieve photoselectivity. This concept, first discussed in Refs. 1 and 2, is illustrated in Fig. 33 for atomic gadolinium in a $J = 2 \rightarrow 2 \rightarrow 1 \rightarrow 0$ excitation and photoionization sequence. In fact, polarization selection rules in resonant photoionization provide a convenient tool for unambiguously determining the angular momentum or J quantum numbers of previously unassigned levels. This is illustrated in the gadolinium autoionization spectra shown in Fig. 34. Here the $J = 0$ autoionization resonances disappear if the quadrupole filter used in the experiment is tuned to any even isotope because parallel linear polarizations were used in the excitation sequence.

The behavior of atomic levels in the presence of external electric and magnetic fields is another area studied extensively in our program. In Figs. 35 and 36 we illustrate some dramatic Stark effects that can be observed for high-lying valence levels even at extremely modest electric fields. The high-resolution spectra were taken with a cw dye laser scanned across the $J = 0$ autoionizing resonance at 49,799 cm^{-1} in ^{160}Gd using the field ionization and collection arrangement shown earlier. These types of data are important to understand and quantify level shifts and line-broadening mechanisms that can be present in extractors used to collect the photoions produced in AVLIS separators.

Perhaps the most important spectroscopic parameters in the AVLIS process are the transition oscillator strengths or dipole moments. The resulting optical cross sections determine the laser fluences needed for effective atomic photoionization. Unfortunately, transition strengths are particularly difficult to measure accurately. This is especially true of bound-bound ground- and excited-state transitions in the heavy elements. Since the inception of the AVLIS program at Livermore, we have investigated many conventional as well as laser techniques for obtaining high-quality data on transition strengths. In addition, we have supported novel schemes suggested by colleagues at other laboratories such as a technique based on ac Stark shifts.

A method used extensively in our laboratories for accurately measuring transition oscillator strengths relies on observing Rabi flopping of atomic populations. An example of data for atomic gadolinium obtained using this technique is shown in Fig. 37. The ^{160}Gd was photoionized in a stepwise fashion by three resonant laser pulses. The first- and second-step excitations were derived from pulse-amplified cw dye laser systems, mentioned above, allowing selective excitation and detection of ^{160}Gd without a quadrupole mass filter. The second and subsequent photoionizing steps were delayed in time from the first-step excitation pulse. In Fig. 37 the photoion signal is plotted as a function of fluence of the first-step laser. The dramatic oscillations observed in the photoion signal arise from the coherent evolution of the atom between the manifold of magnetic sublevels in the ground and first excited state. Since each magnetic sublevel has its own dipole moment, the signal is not purely sinusoidal as a function of field amplitude of the first-step laser, but is instead periodic. This is indeed the case if the photoion signal is plotted against the square root of the fluence. Instead, we plot the theoretical signal as a function of fluence for the appropriate laser polarizations and level J values employed in the experiment. Since the first-step laser fluence is accurately measured, the only parameter varied to fit the data is the transition oscillator strength. This method has been used in our laboratory to measure transition oscillator strengths for bound-bound transitions originating on both low- and high-J excited states.

As discussed earlier, the program at Livermore originally focused on laser isotope separation of atomic uranium because of the large demand and high product enrichment price for material used as fuel in commercial light-water nuclear power reactors. In support of that effort, we adopted a fundamental approach to photoionization physics and developed spectroscopic techniques to obtain the necessary data base. We believe that once fully developed and deployed for uranium, the AVLIS process can be applied directly to separating many elements economically on an industrial scale. The spectroscopic data bases for candidate elements such as gadolinium, using the methods described above, are being vigorously pursued in our program.

It has taken about 12 y for the AVLIS program to reach its current state of maturity. We are presently in a production-scale systems-integration stage, having completed process science studies and developed and tested the laser and separator subsystems in stand-alone as well as in fully integrated enrichment operations.

We have just activated a full-scale demonstration facility. The building houses a uranium separator module called the separator demonstration facility. The building also contains a laser system called the laser demonstration facility that will provide the laser power for the module. The balance of the building contains instrumentation and control systems and refurbishment facilities in support of the laser and separator systems.

Figure 38 shows the first completed corridor of copper-vapor MOPA chains installed in the facility in April 1985. There are 6 MOPA chains containing 30 laser heads with a total output capability of several thousand watts. Figure 39 shows the optical system in the dye laser corridor and Fig. 40 shows a large dye laser amplifier in the facility.

Figure 41 shows the separator module in the full-scale demonstration facility. The tanks at the ends house the module optics for directing the laser beams through the uranium vapor. The module is essentially plant size and has a projected production rate of about 1 X 10^6 SWU/y, or 200 Mg product/y.

For the past several years we have transported the output of the laser subsystems over long distances (~1 km) to separator subsystems located in other buildings. Using the initial increment of light available from our new laser facility, we have recently conducted integrated enrichment demonstrations in our half-scale facility shown in Fig. 42. This facility has been operational for several years.

As a final note, dozens of scientists, engineers, and supporting staff have committed over a decade of their lives in trying to bring this technology to industrial scale. With the recent decision made by the Department of Energy to make AVLIS the technology of the 21st century, we are well on our way. We hope the rest of the laser and electro-optics community will share in the excitement and challenge this will offer for the future of laser-driven processes.

REFERENCES

1. Ya.B. Zel'dovich and I.I. Sobel'man, "Optical Excitation of Isotopes That Are Selective in Nuclear Spin, JETP Lett. 21 (6) 168-169 (1975).

2. L.C. Balling and J.J. Wright, "Use of Angular Momentum Selection Rules for Laser Isotope Separation," Appl. Phys. Lett. 29 (7), 411-413 (1976).

Atomic vapor laser isotope separation – major systems

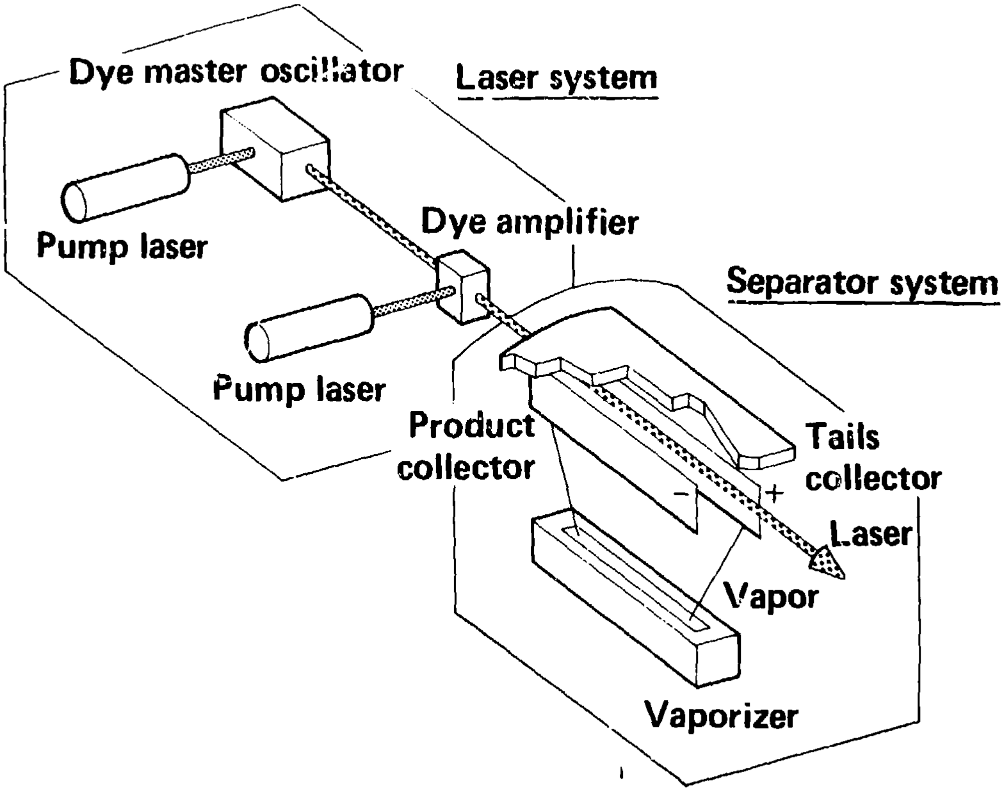

30-01-0681-1562A

Fig. 1

Candidate elements for processing using atomic vapor laser isotope separation

Element	Application	Demand (Mg/y)
Uranium	Low-cost fuel for light-water reactors	>1000
Samarium Europium Gadolinium, etc.	Burnable poison for power reactors	>1
Mercury	More efficient fluorescent lamps	>1
Zirconium	Cladding for nuclear-fuel elements	>1
Rhodium Palladium Platinum	Precious-metal recovery from nuclear waste	>1

Fig. 2

Estimate of world demand for uranium enrichment

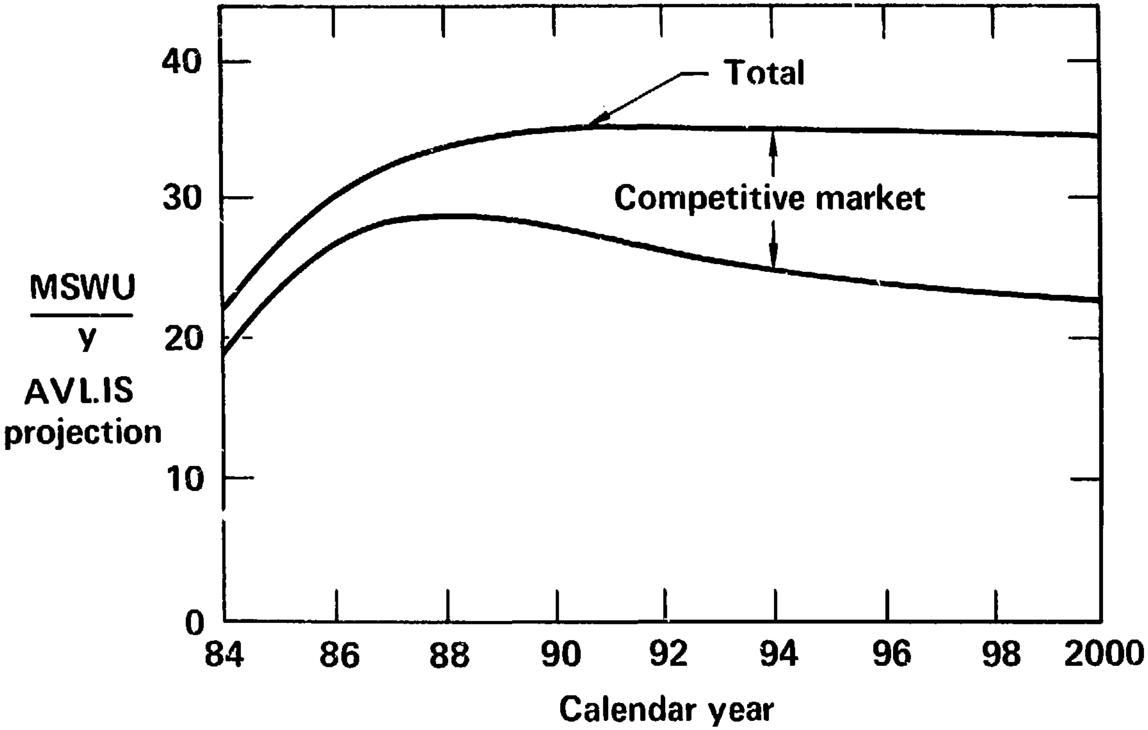

30-90 1085-4509

Fig. 3

Competitive range of prices for uranium enrichment

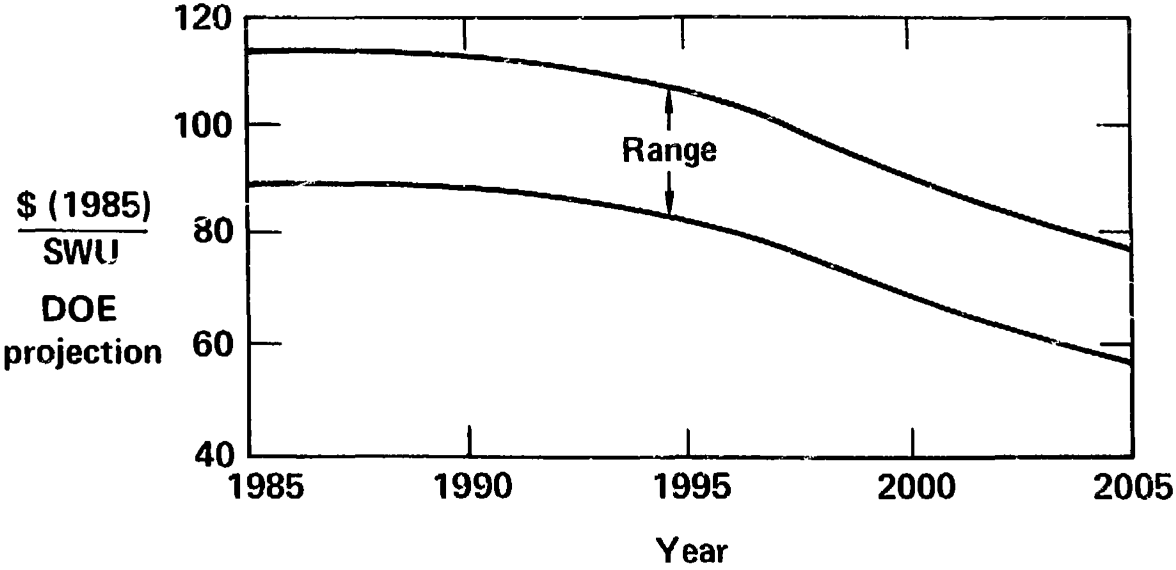

Market size (2000) — AVLIS projection

Domestic total ~ 900 M$/y

Competitive market ≳ 1000 M$/y

30 90 1085·4510

Fig. 4

Separative work units

$$\text{SWU (kg)} = \text{Product (kg)} \cdot V(X_p)$$
$$+ \text{Tails (kg)} \cdot V(X_T)$$
$$- \text{Feed (kg)} \cdot V(X_F)$$
$$V(X) = (2X - 1) \ln\left(\frac{X}{1 - X}\right)$$
$$X = \text{wt fraction } {}^{235}\text{U}$$

At "standard" conditions

$X_F = 0.00711$

$X_P = 0.032$

$X_T = 0.002$

1 SWU converts 1.24 kg of feed into 0.21 kg of product

In this case, operation at $\lesssim$ \$60/SWU requires enrichment at a cost of

$<$ \$49/kg feed

$<$ \$286/kg product

Elements of separative work cost

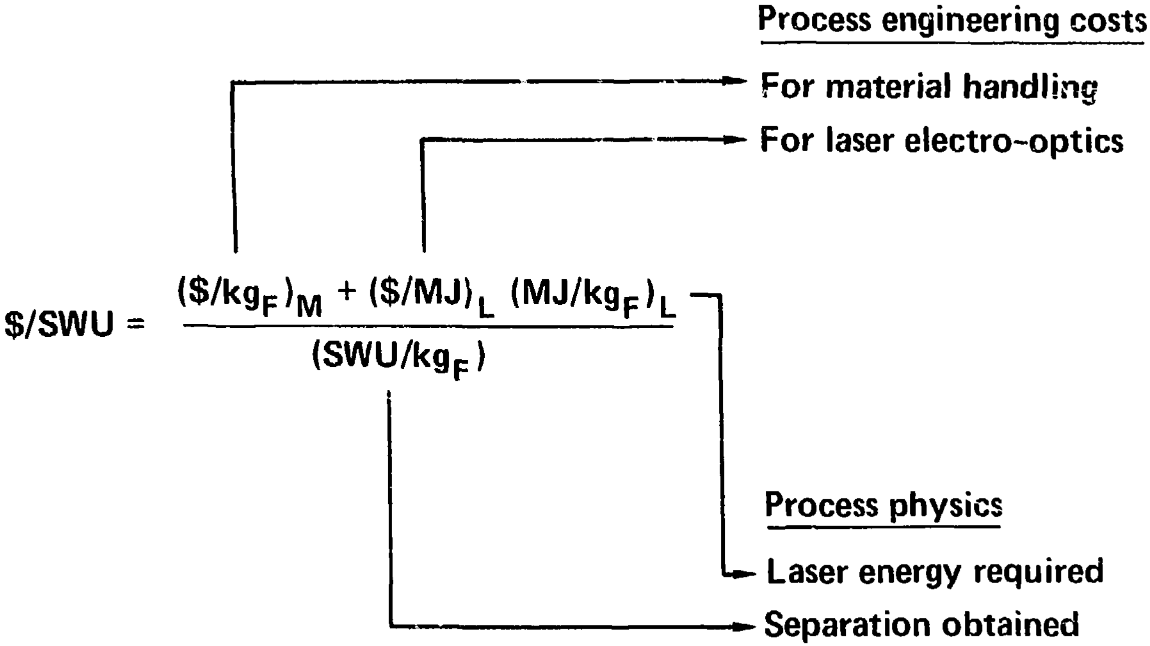

$$\$/\mathrm{SWU} = \frac{(\$/\mathrm{kg_F})_M + (\$/\mathrm{MJ})_L\ (\mathrm{MJ/kg_F})_L}{(\mathrm{SWU/kg_F})}$$

Process engineering costs

For material handling

For laser electro-optics

Process physics

Laser energy required

Separation obtained

30 90 1085 4512

Fig. 6

Laser figures of merit

$$(\mathrm{MJ/kg_F}) = \underbrace{\frac{1}{\epsilon}}_{\substack{\text{Photon}\\ \text{utilization}\\ (0.2)}} \times \underbrace{h\nu}_{\substack{\text{Photon energy}\\ \text{(all steps)}\\ (6)}}\left(\frac{\mathrm{eV}}{\mathrm{atom}}\right) \times 1.6 \times 10^{-25}\left(\frac{\mathrm{MJ}}{\mathrm{eV}}\right) \times \frac{6 \times 10^{26}}{\underbrace{\mathrm{MW}}_{\substack{\text{Molecular}\\ \text{weight}\\ (238)}}}\left(\frac{\mathrm{atoms}}{\mathrm{kg_F}}\right) \times [\underbrace{X_F}_{\substack{\text{Mole fraction}\\ \text{of desired}\\ \text{isotope}\\ (0.007)}} + \underbrace{\frac{1}{S}}_{\substack{\text{Photo-}\\ \text{selectivity}\\ (> 10^4)}}(1 - X_F)]$$

$$(\mathrm{MJ/kg_F}) \lesssim 0.1 \text{ for uranium AVLIS}$$

$(\$/\mathrm{MJ})_L \lesssim \$100$ for an engineered electro-optics system

$\therefore (\$/\mathrm{kg_F})_L \lesssim \$10$ for uranium AVLIS

- High selectivity is essential to achieve low $\mathrm{MJ/kg_F}$
  - Obtained in AVLIS

Fig. 7

Separative work performance

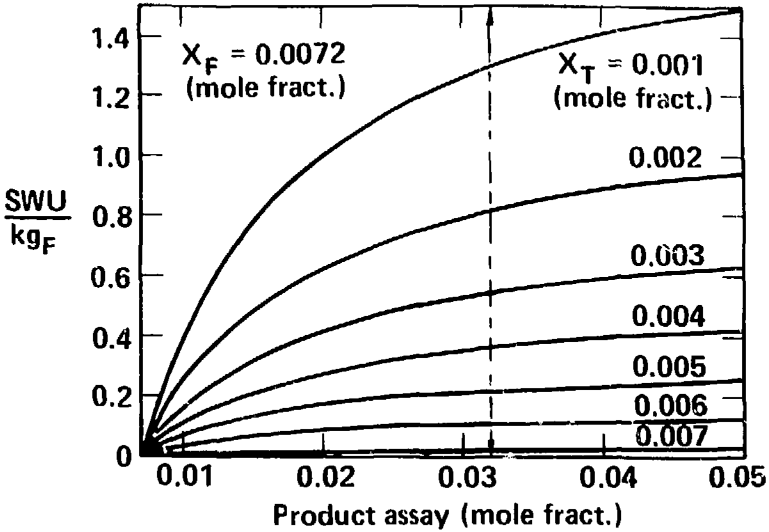

- High SWU/kg_F corresponds to low tails assay

- Design goal for process physics is efficient stripping of the ^{235}U atoms from the feed stream

30-00-0585-1943A

AVLIS process steps

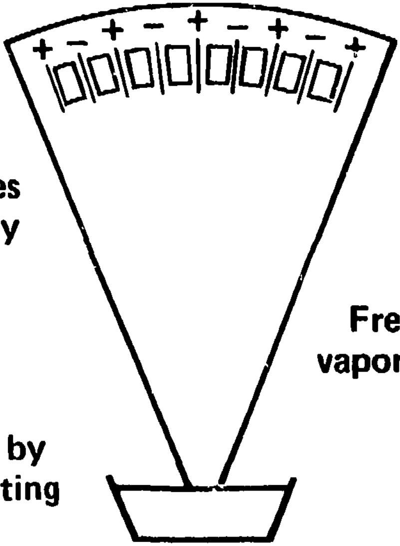

Product and tails withdrawn
as liquid in continuous process

Remaining vapor
flows to roof as tails

Ions are drawn to
negative bias on
extractor as product

Superimposed pulses
of 3 lasers selectively
photoionize vapor

Free expansion converts
vapor to cooled hypersonic
flow

Vapor generated by
electron-beam heating

Fig. 9

Vaporization phenomena

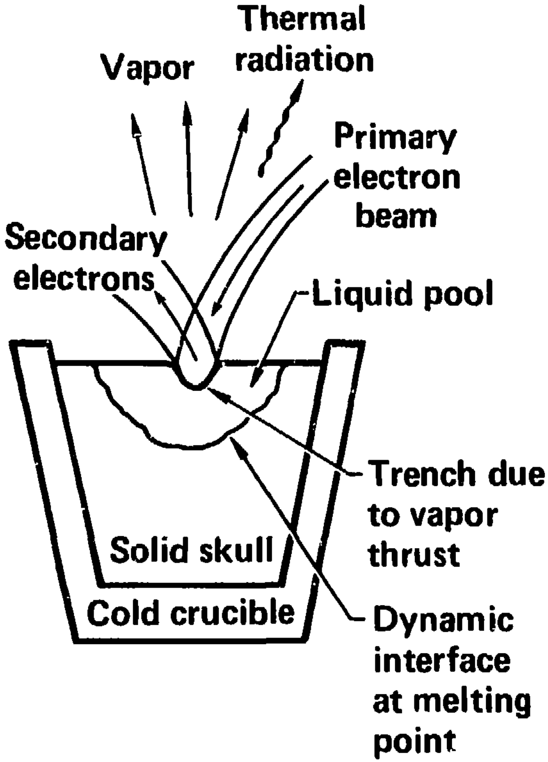

Objective:

Maximize vaporization efficiency (g of vapor/kWh of electron-beam energy)—i.e., maximum T rise from crucible to hot zone

Observation:

Temperature dependence of density (buoyancy) and surface tension sets up convection cells in liquid pool, enhancing heat transfer to crucible

Fig. 10

Liquid-pool modeling

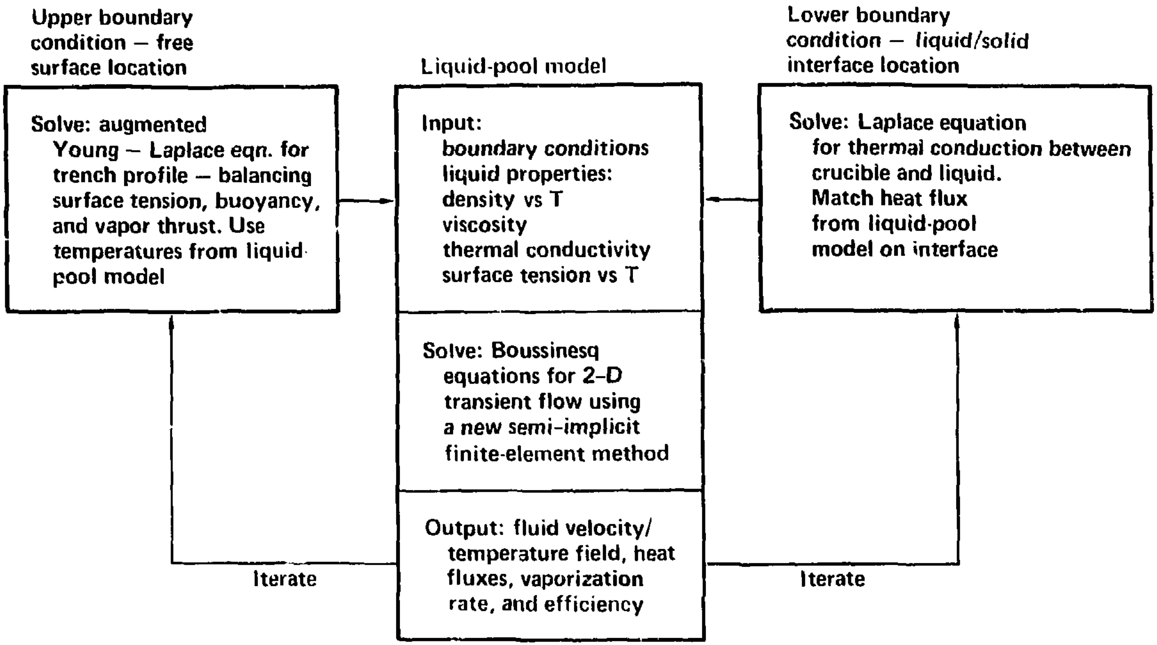

Upper boundary condition – free surface location

Solve: augmented Young – Laplace eqn. for trench profile – balancing surface tension, buoyancy, and vapor thrust. Use temperatures from liquid-pool model

Liquid-pool model

Input:
boundary conditions
liquid properties:
density vs T
viscosity
thermal conductivity
surface tension vs T

Solve: Boussinesq equations for 2-D transient flow using a new semi-implicit finite-element method

Output: fluid velocity/temperature field, heat fluxes, vaporization rate, and efficiency

Lower boundary condition – *liquid/solid* interface location

Solve: Laplace equation for thermal conduction between crucible and liquid. Match heat flux from liquid-pool model on interface

30-90-1085-4514

Fig. 11

Liquid-pool model — time dependence/tests

Time dependence:

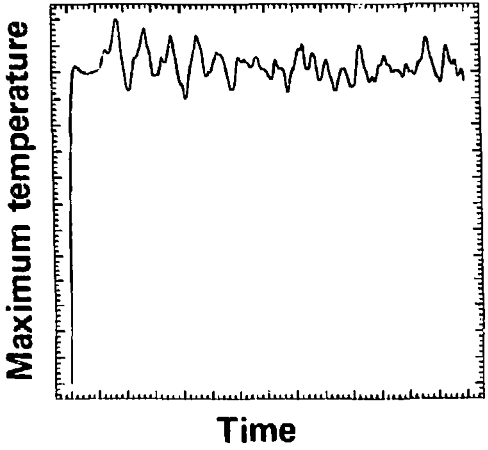

Flow is predicted to be laminar and chaotic

Tests: Pool model using lower boundary from post-run (frozen) sections in qualitative agreement with:

- Free surface velocity from cinematography
- Hot-zone temperatures from total vapor energy

Vapor properties of interest

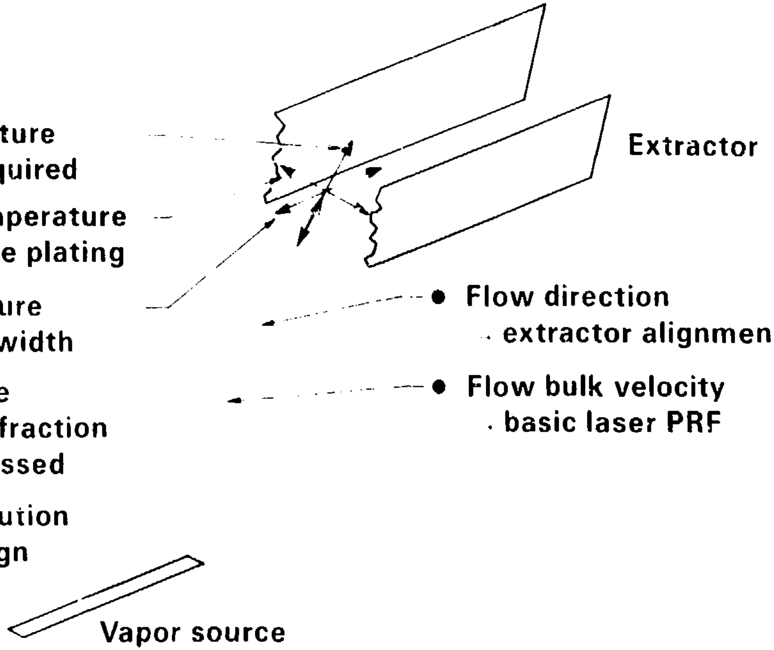

- Radial temperature
  - Over PRF required
- Transverse temperature
  - Non-selective plating
- Axial temperature
  - Doppler linewidth
- Electronic state populations · fraction of atoms addressed
- Density distribution
  - system design

- Flow direction
  - extractor alignment
- Flow bulk velocity
  - basic laser PRF

Fig. 13

Transition flow modeling

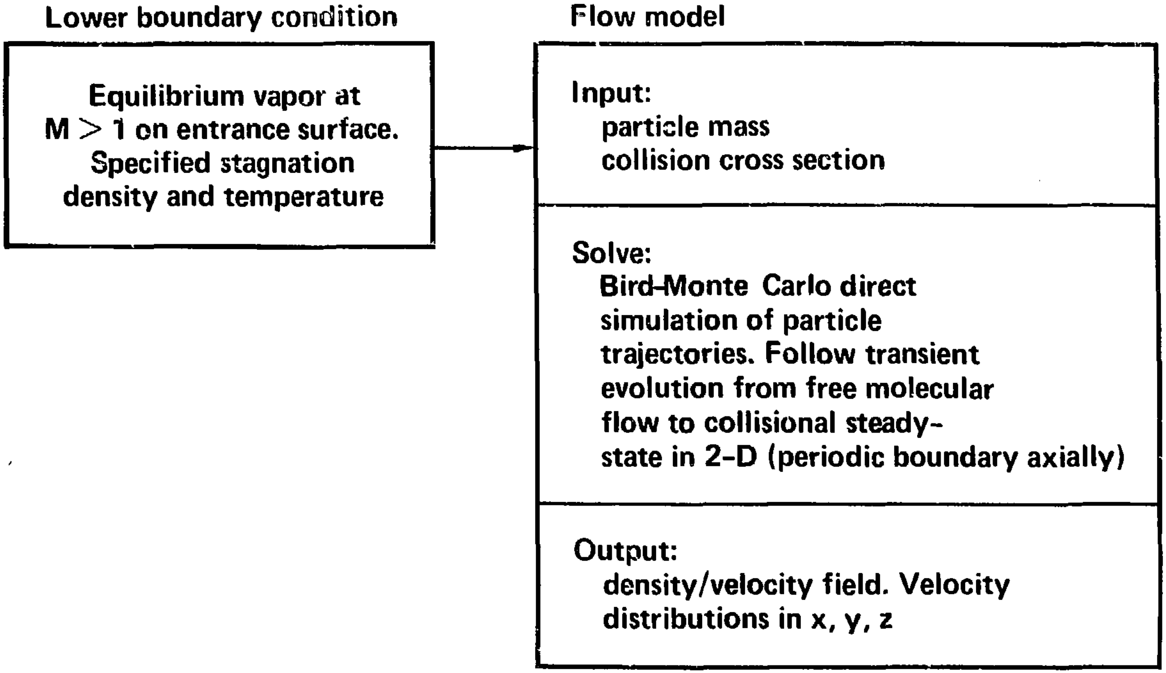

Lower boundary condition

Equilibrium vapor at
$M > 1$ on entrance surface.
Specified stagnation
density and temperature

Flow model

Input:
- particle mass
- collision cross section

Solve:
Bird-Monte Carlo direct simulation of particle trajectories. Follow transient evolution from free molecular flow to collisional steady-state in 2-D (periodic boundary axially)

Output:
density/velocity field. Velocity distributions in x, y, z

Fig. 14

Characteristic evolution of transverse velocity distributions

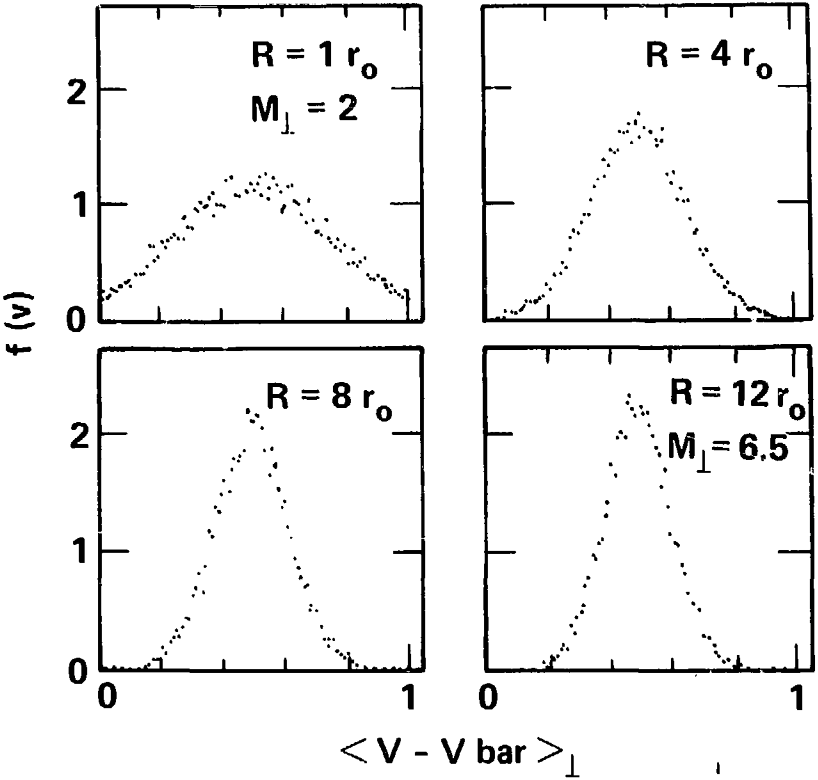

Cylindrical
expansion
He, Kn = 0.003

Velocities in
all plots
normalized to
1.9364×10^5 cm/s

30-90-1085-4516

Fig. 15

Temperatures in transition flow

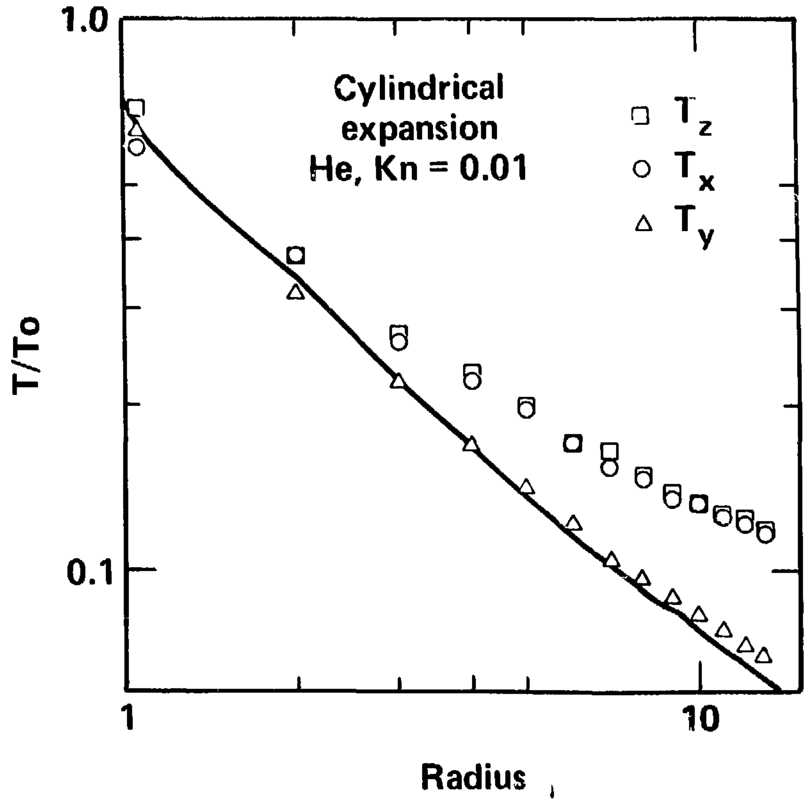

Fig. 16

Diagnostic Laser

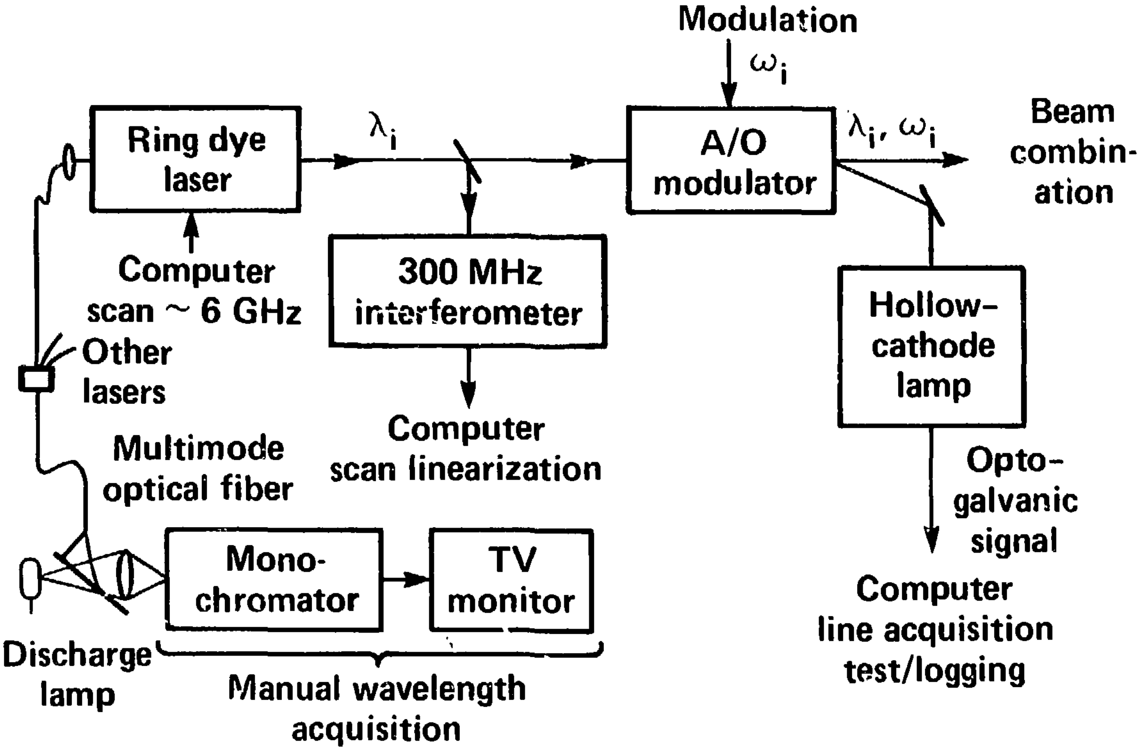

30-90-1085-4522

Fig. 17

Diagnostic Laser System

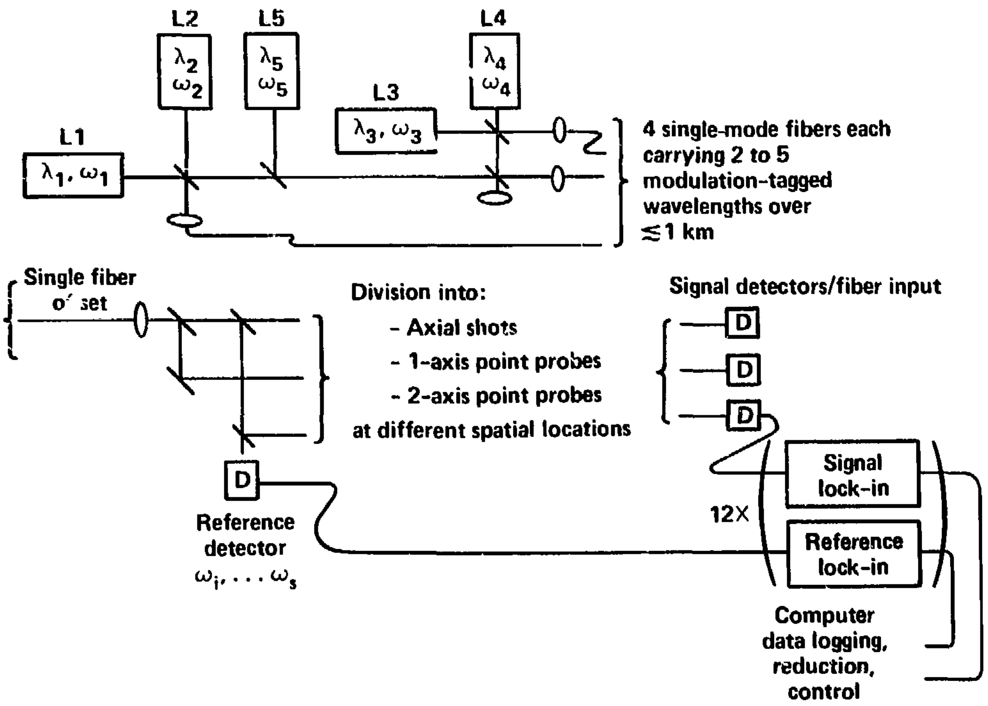

30-90-1085-4523

Axial laser diagnostics

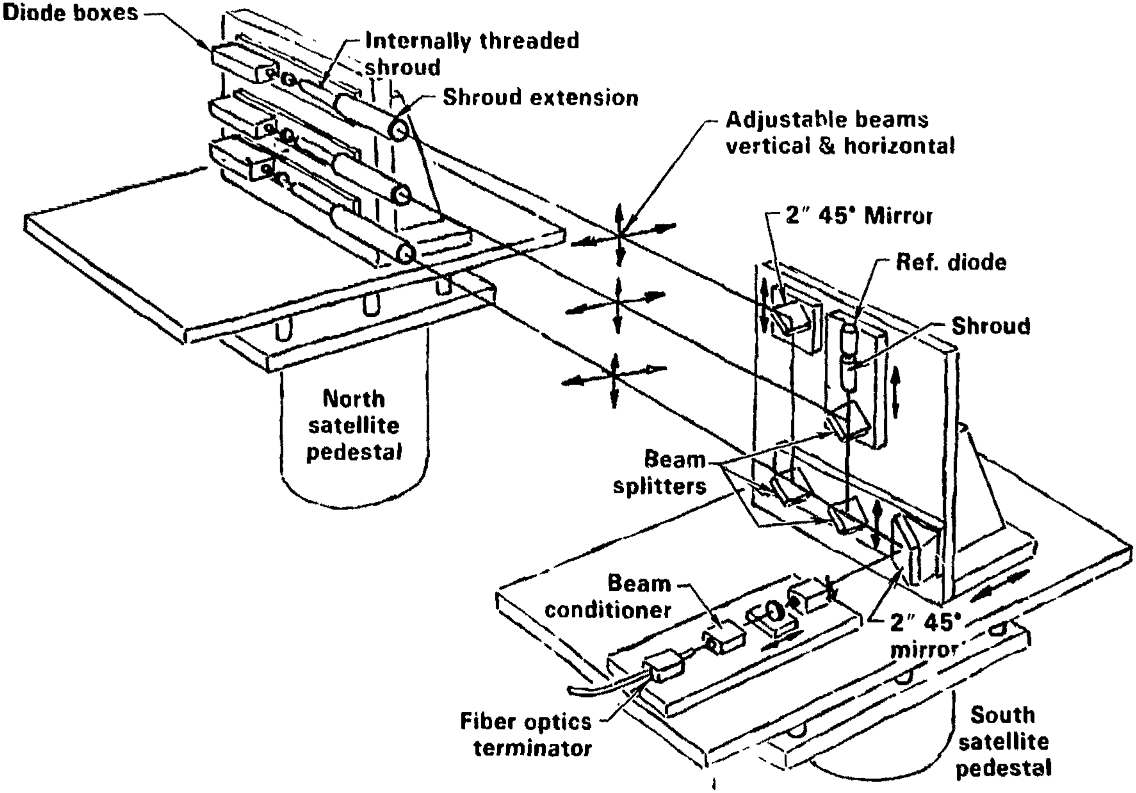

30-90-1085-4531

CCG 11-16-82

Fig. 19

Point probe diagnostics

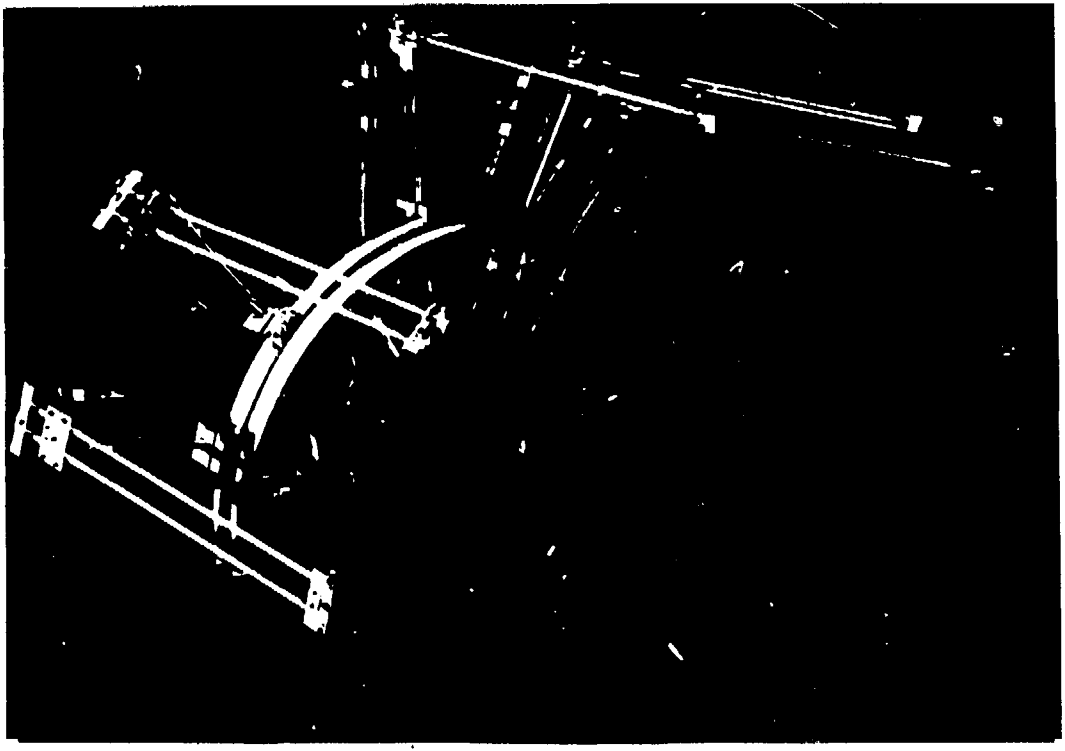

Fig. 20

Real-time reduction of laser measurements

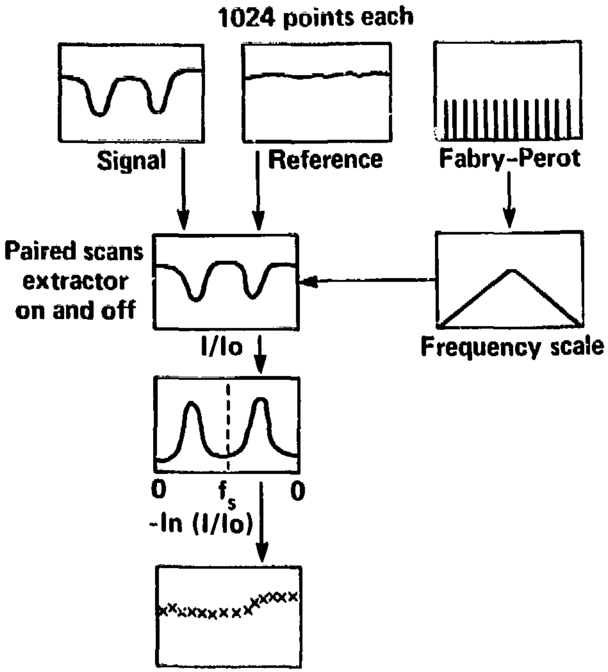

Perform scan	2 s
Test for satisfactory operating condition	2 s
Transfer to computer workspace	
Generate frequency scale	1 s
Remove background	
Acquire L, λ, σ from relational data base	
Generate absorption trace	
Least-squares fit Gaussian line shape. Test for valid scan	
Calculate line width, Mach numbers, state populations, total density, ion density, etc.	
Display variables to control room as time histories or cross plots -on demand	2 s

Fig. 21

Console display of neutral and ion densities

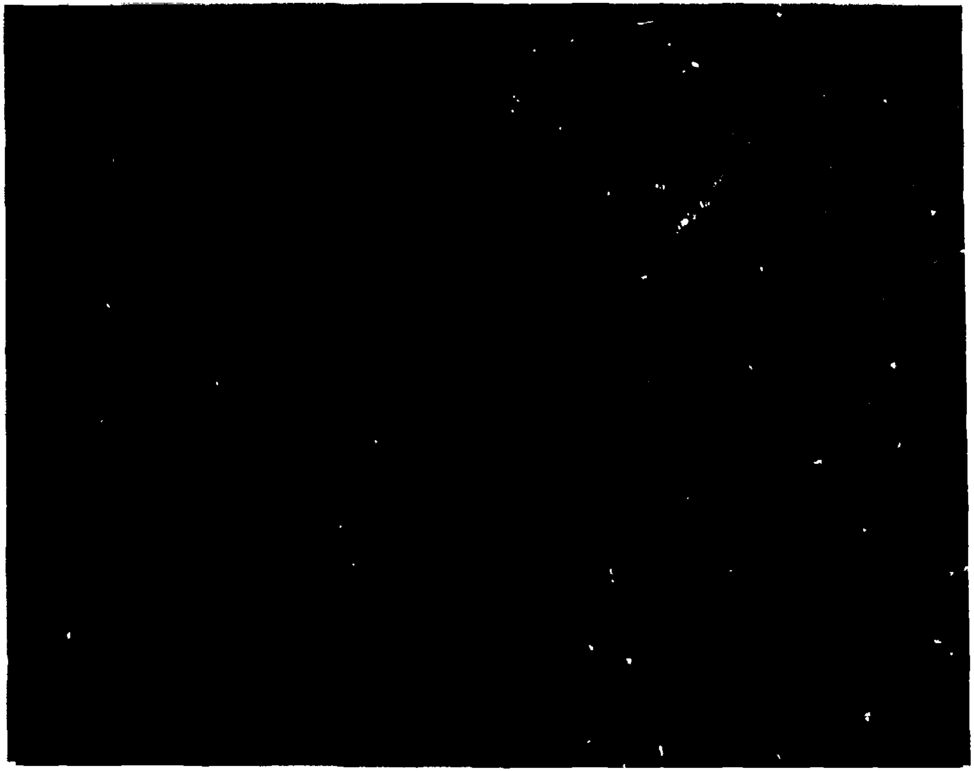

Fig. 22

Laser measurement of bulk flow velocity — point probe

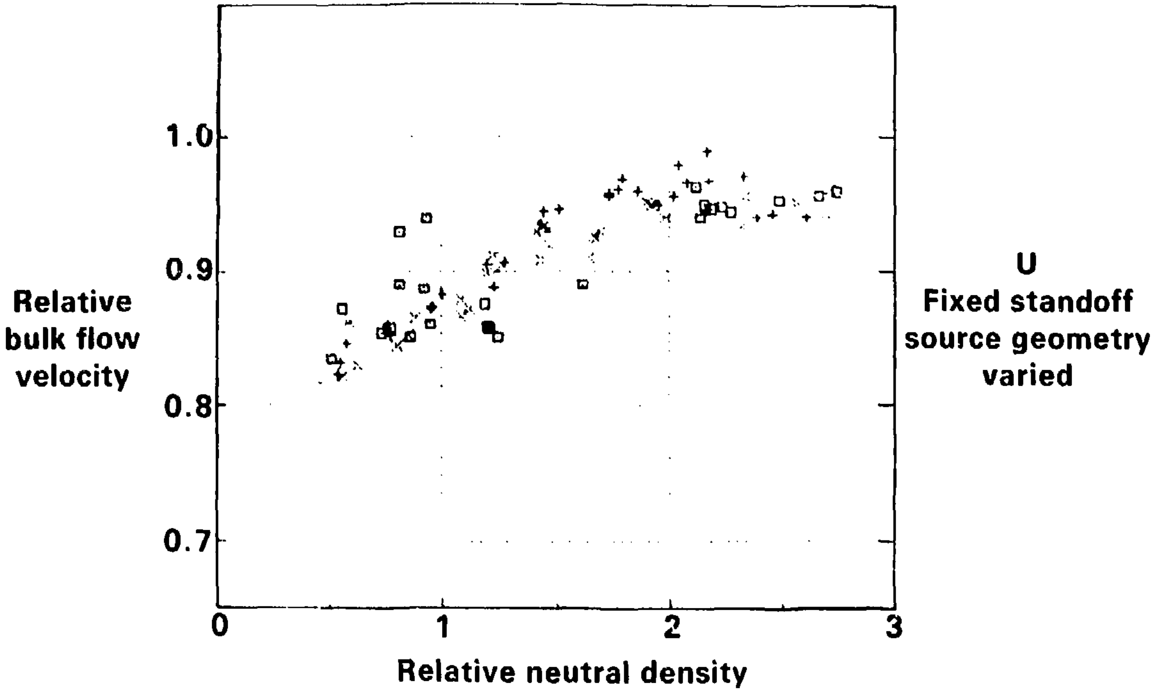

30-90-1085-4534

Fig. 23

Laser measurement of electronic state populations — axial probe

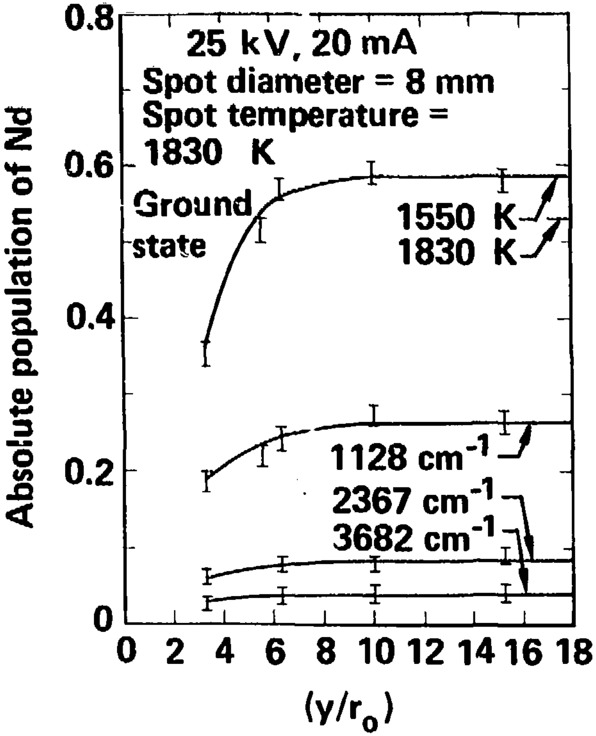

Nd

State populations vs. standoff (y) scaled to source diameter (r_o)

H.-L. Chen, R. Bedford, C. Borzileri, W. Brunner and M. Hays
J. Appl. Phys. 49, 6136 (78)

30-90-1085-4524

Modeling of laser – atomic vapor interaction

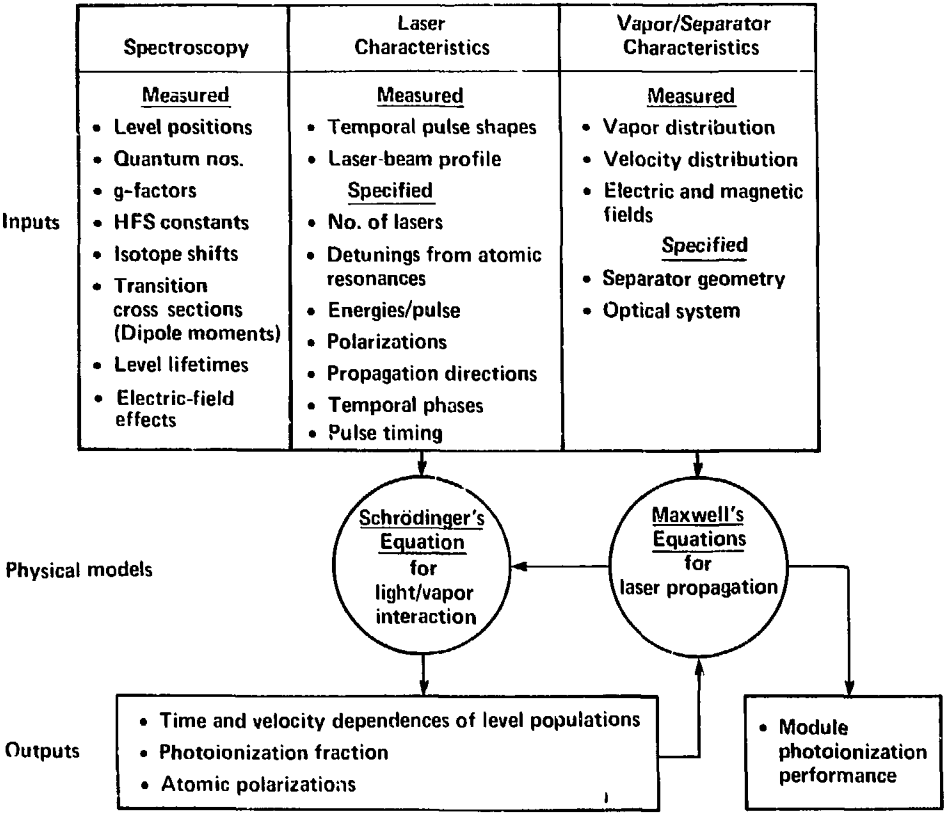

Inputs

Spectroscopy	Laser Characteristics	Vapor/Separator Characteristics
Measured • Level positions • Quantum nos. • g-factors • HFS constants • Isotope shifts • Transition cross sections (Dipole moments) • Level lifetimes • Electric-field effects	Measured • Temporal pulse shapes • Laser-beam profile Specified • No. of lasers • Detunings from atomic resonances • Energies/pulse • Polarizations • Propagation directions • Temporal phases • Pulse timing	Measured • Vapor distribution • Velocity distribution • Electric and magnetic fields Specified • Separator geometry • Optical system

Physical models

<u>Schrödinger's Equation</u> for light/vapor interaction

<u>Maxwell's Equations</u> for laser propagation

Outputs

- Time and velocity dependences of level populations
- Photoionization fraction
- Atomic polarizations

- Module photoionization performance

Fig. 25

SHUX photoionization code example: 3-step, J = 2→2→1→0 photoionization sequence in ^{157}Gd

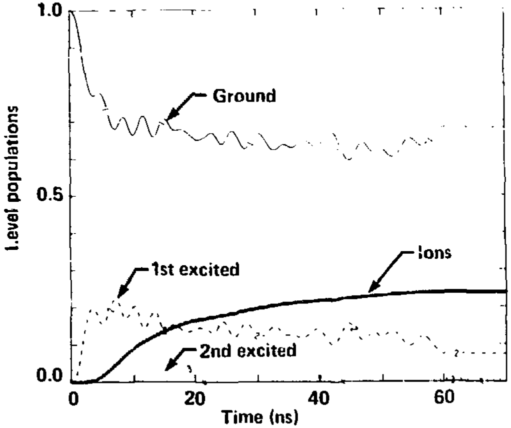

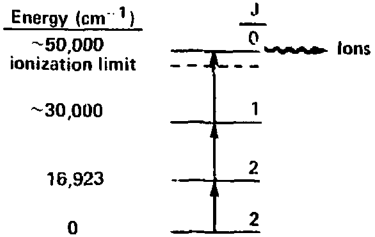

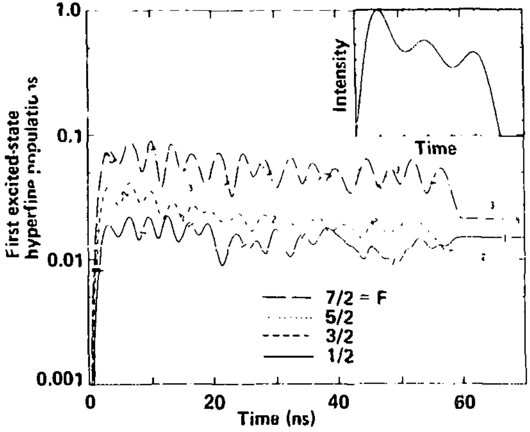

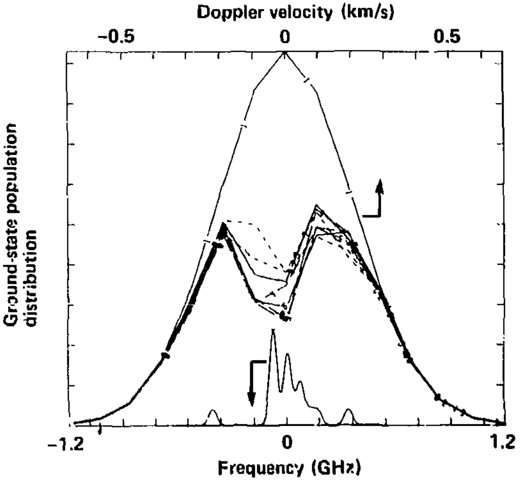

Fig. 26

Experimental layout

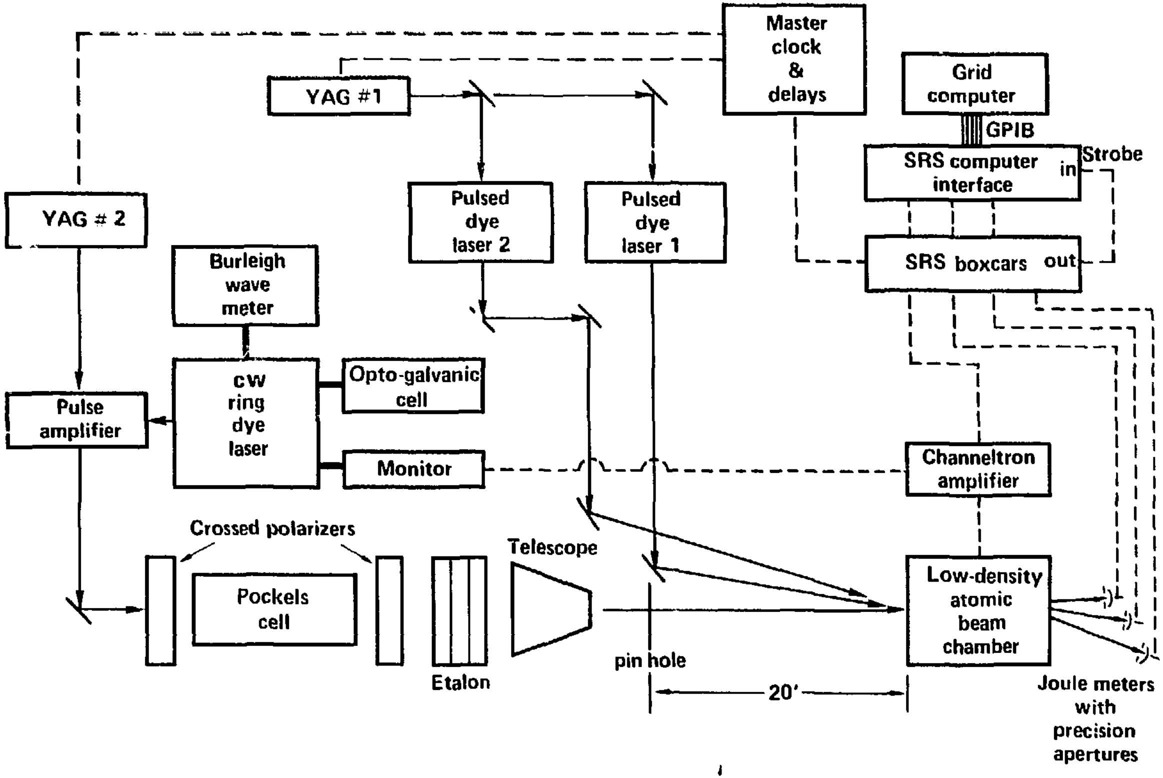

30-90-0885-3609A

Fig. 27

Three stage pulse amplified CW dye laser systems

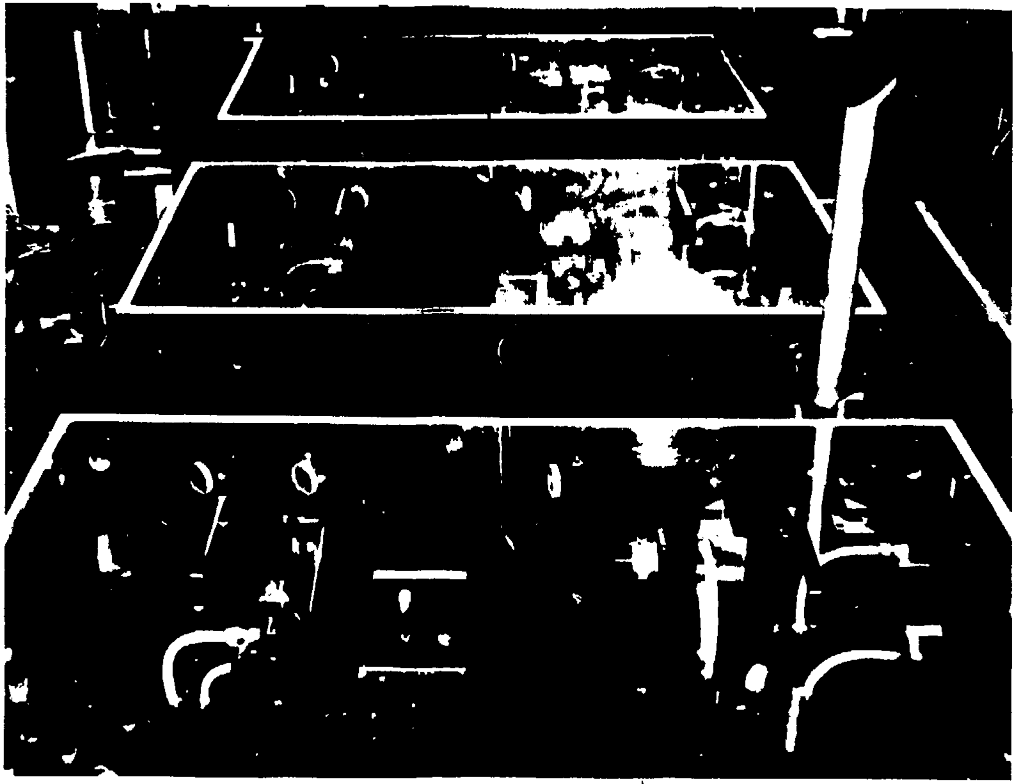

30-10 0683 2051A

10/85

Fig. 28

Atomic beam system used in spectroscopic studies

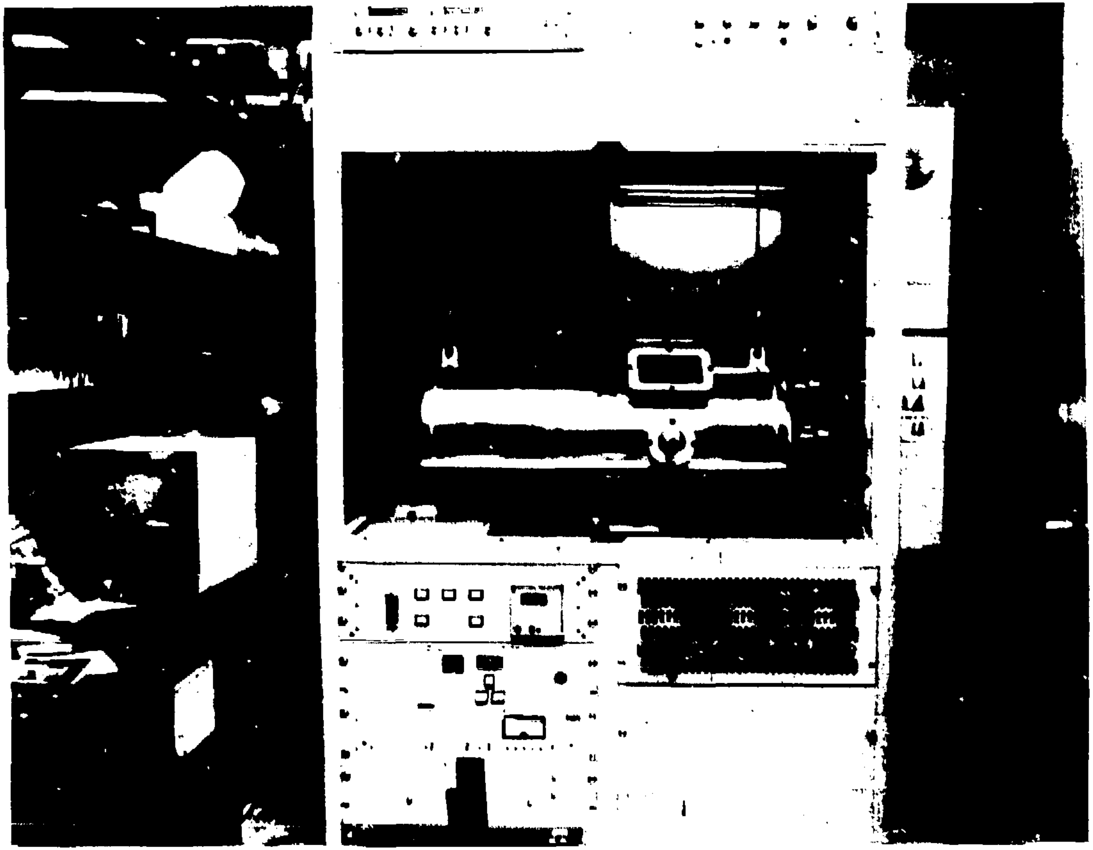

Fig. 29

Schematic of basic components in atomic beam systems

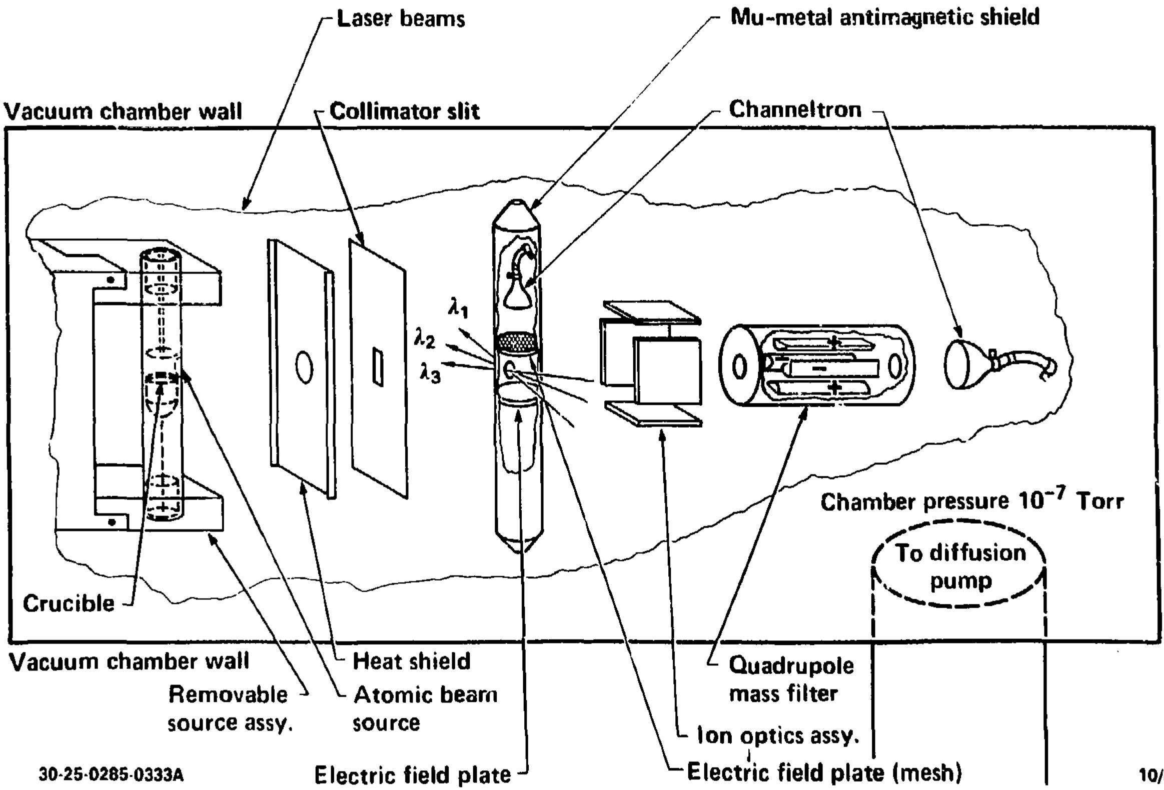

30-25-0285-0333A

10/85

Fig. 30

Lifetime measurement of 17380.8 cm^{-1} level in atomic gadolinium using time delayed photoionization

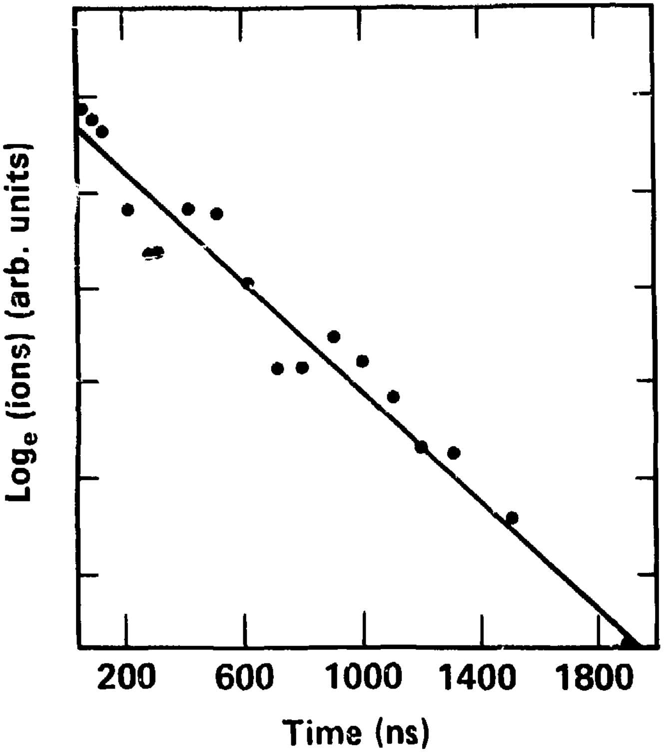

Populate first excited state

Delay 2nd and 3rd laser pulse

τ = 710 ± 100 ns

Fig. 31

Hyperfine structure and isotope shifts for the $215 \rightarrow 17380\ \mathrm{cm}^{-1}$ transition in atomic gadolinium

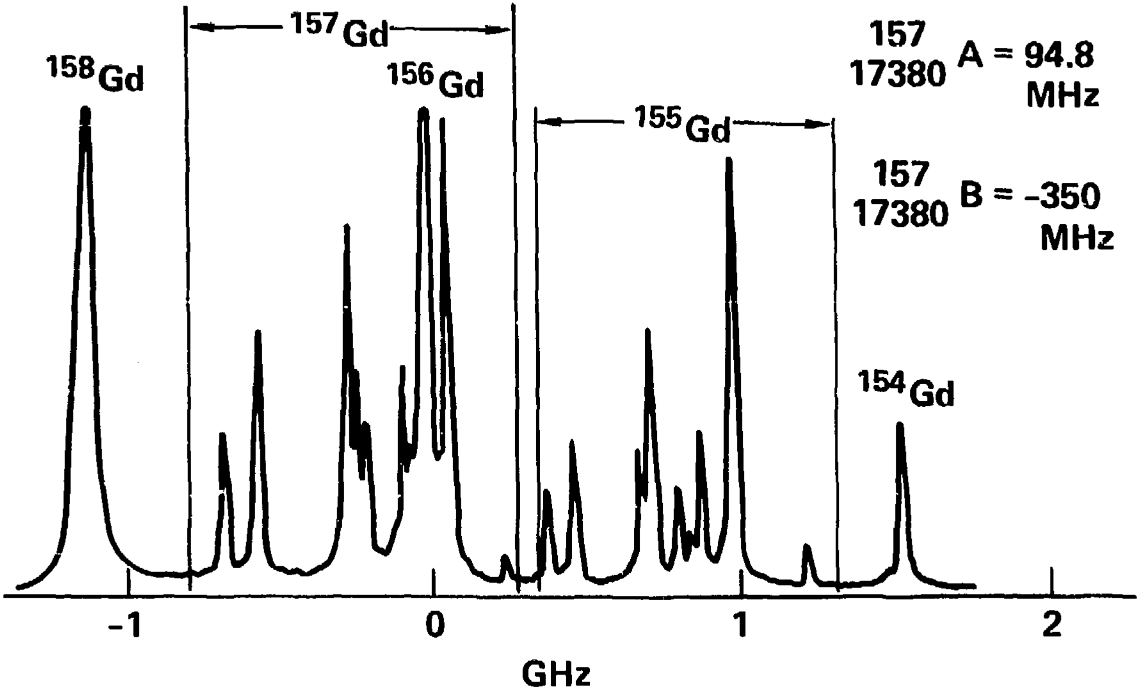

$A^{157}_{17380} = 94.8$ MHz

$B^{157}_{17380} = -350$ MHz

30-90-1085-4525

Fig. 32

Isotopic selectivity in atomic gadolinium using polarized broadband lasers

Parallel linear

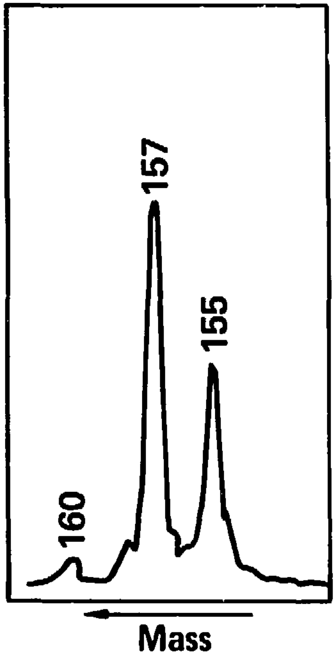

J = 2→2→1→0
Excitation sequence

$\lambda_3 \perp$ to λ_1 and λ_2

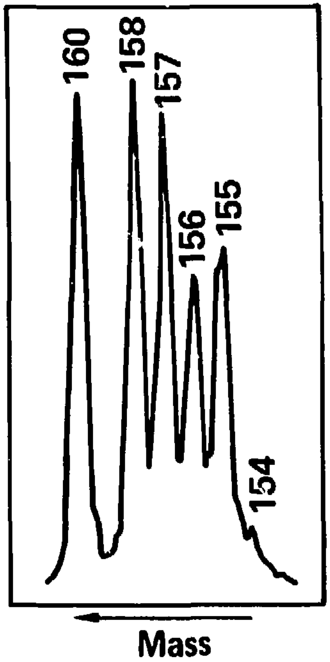

Fig. 33

Autoionization scan from the 32660 cm $^{-1}$ level in atomic gadolinium

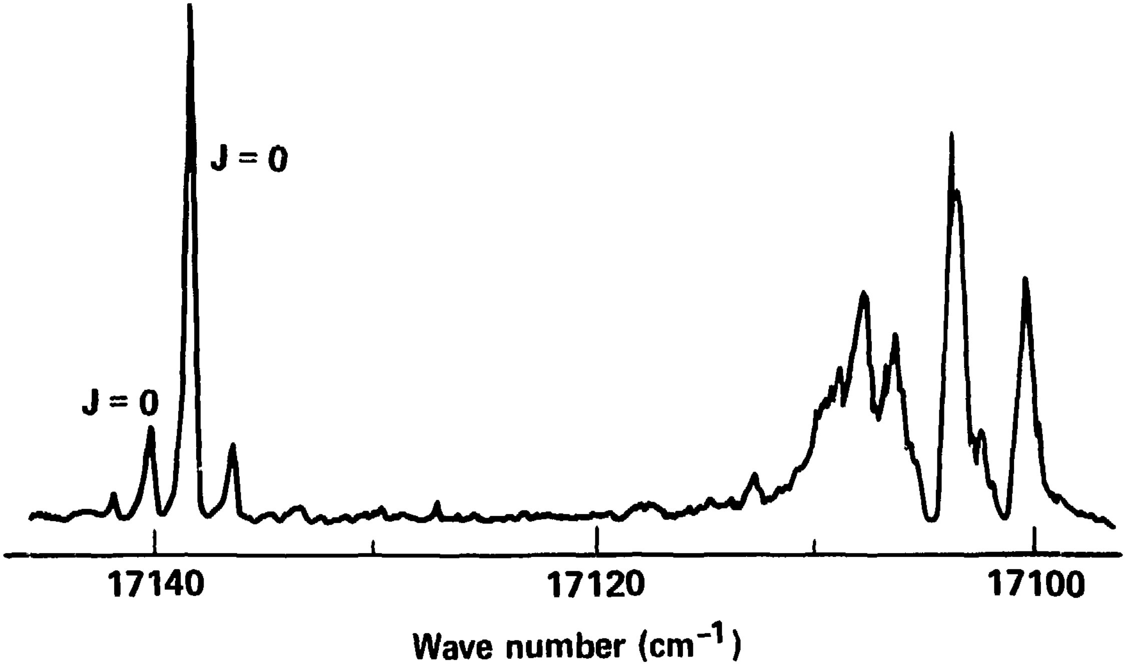

30-90-1085-4527

Fig. 34

DC field effect on the 32660 – 49799 cm^{-1} transition in ^{160}Gd

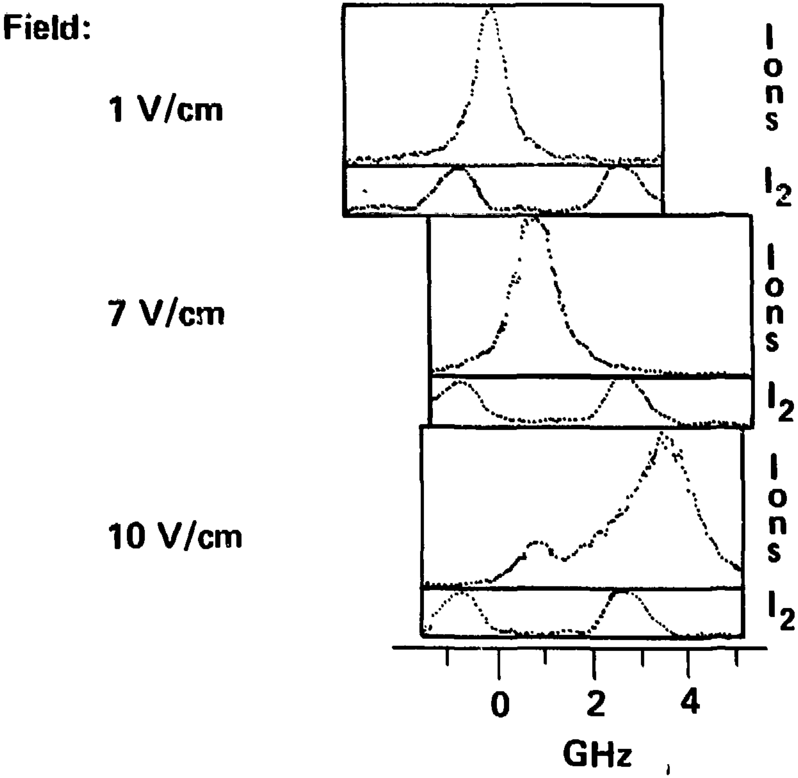

Fig. 35

DC field effect on the 32660 - 49799 cm^{-1} transition in ^{160}Gd

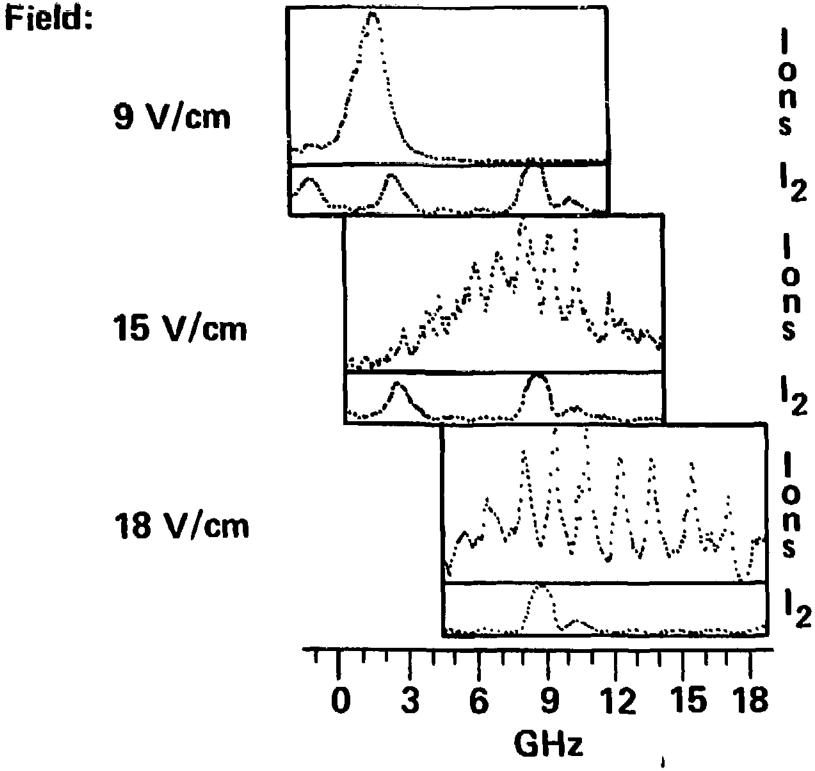

30-90-1085-4529

Fig. 36

Cross section measurement using Rabi oscillations in ^{160}Gd

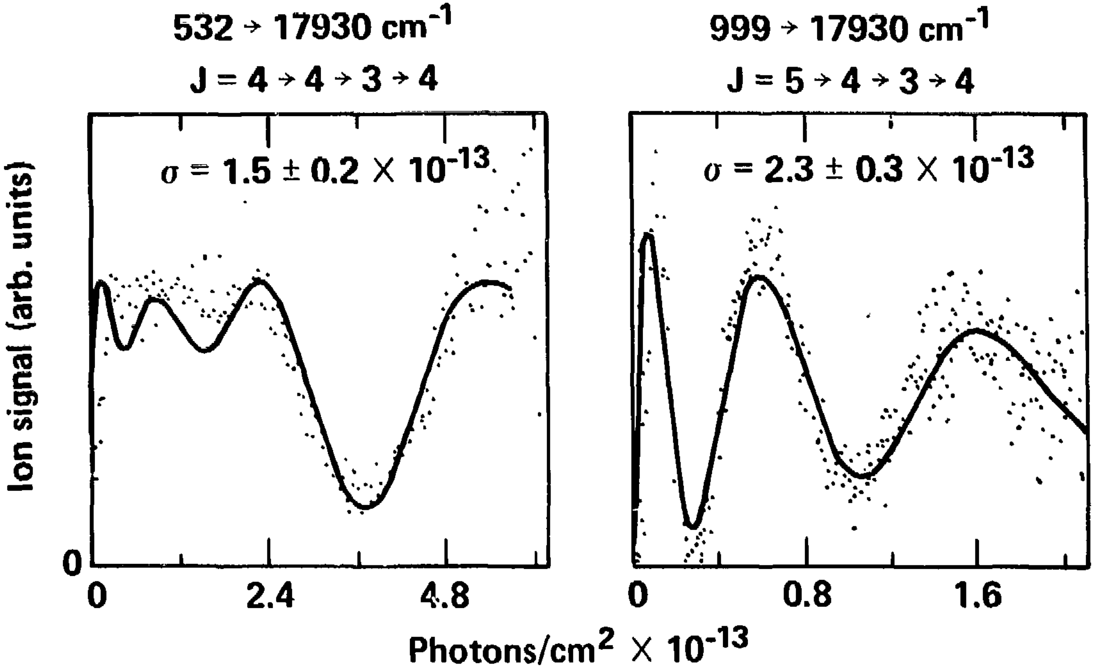

30-90-1085-4530

Fig. 37

LDF corridor with copper-vapor MOPA chains

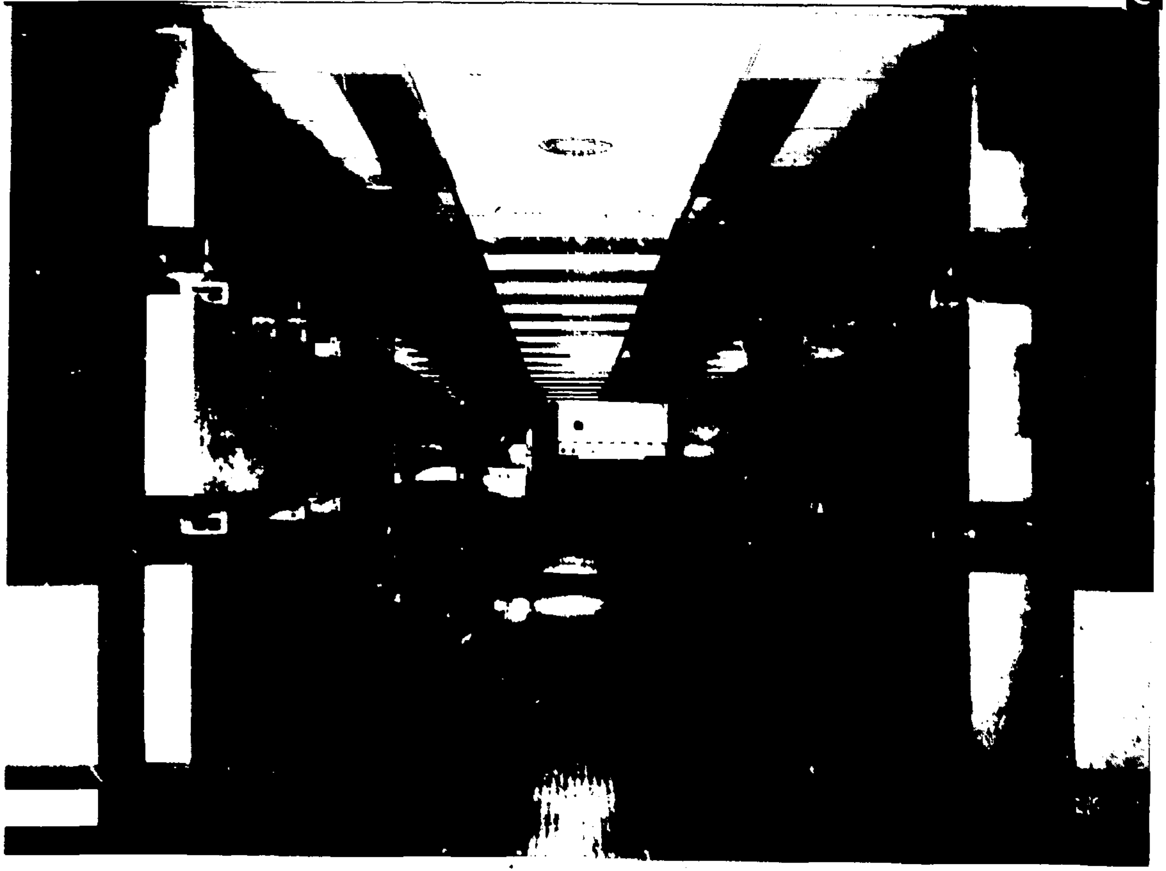

Fig. 38

Optical system in dye laser corridor

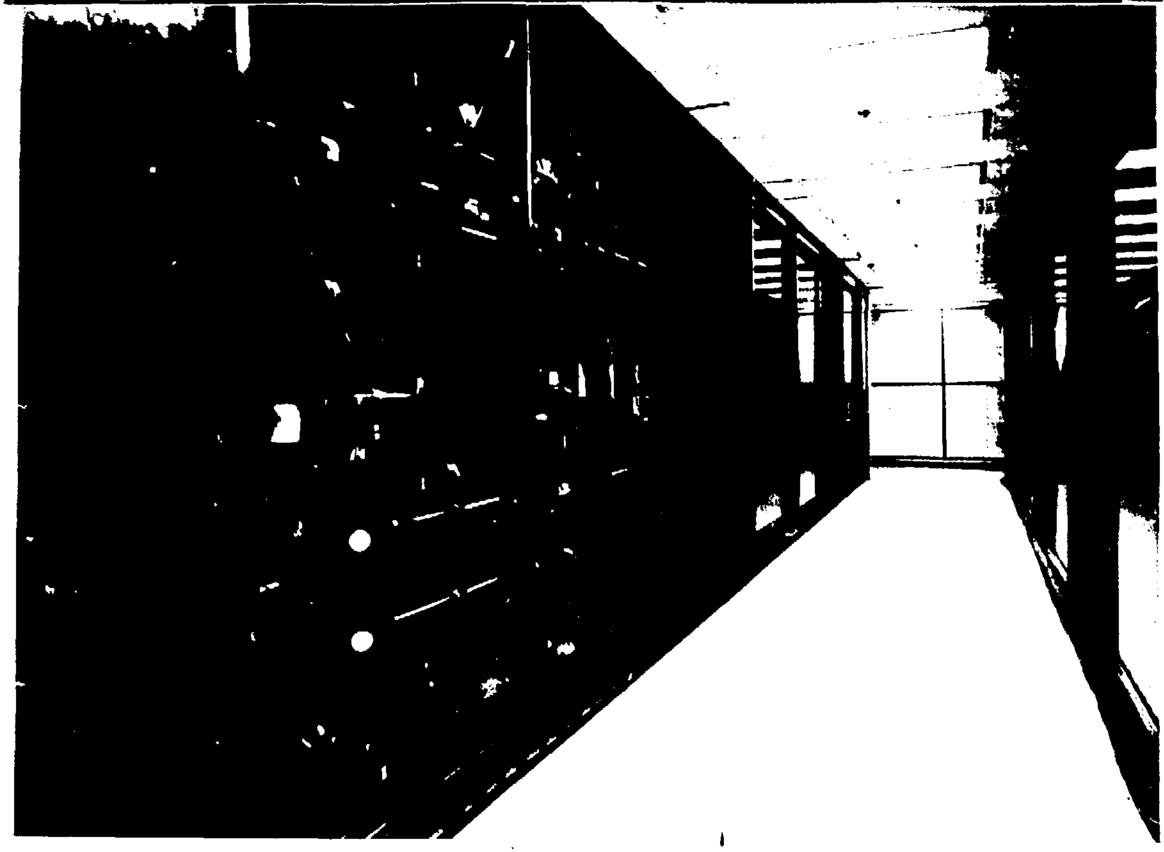

Fig. 39

Large dye laser amplifier

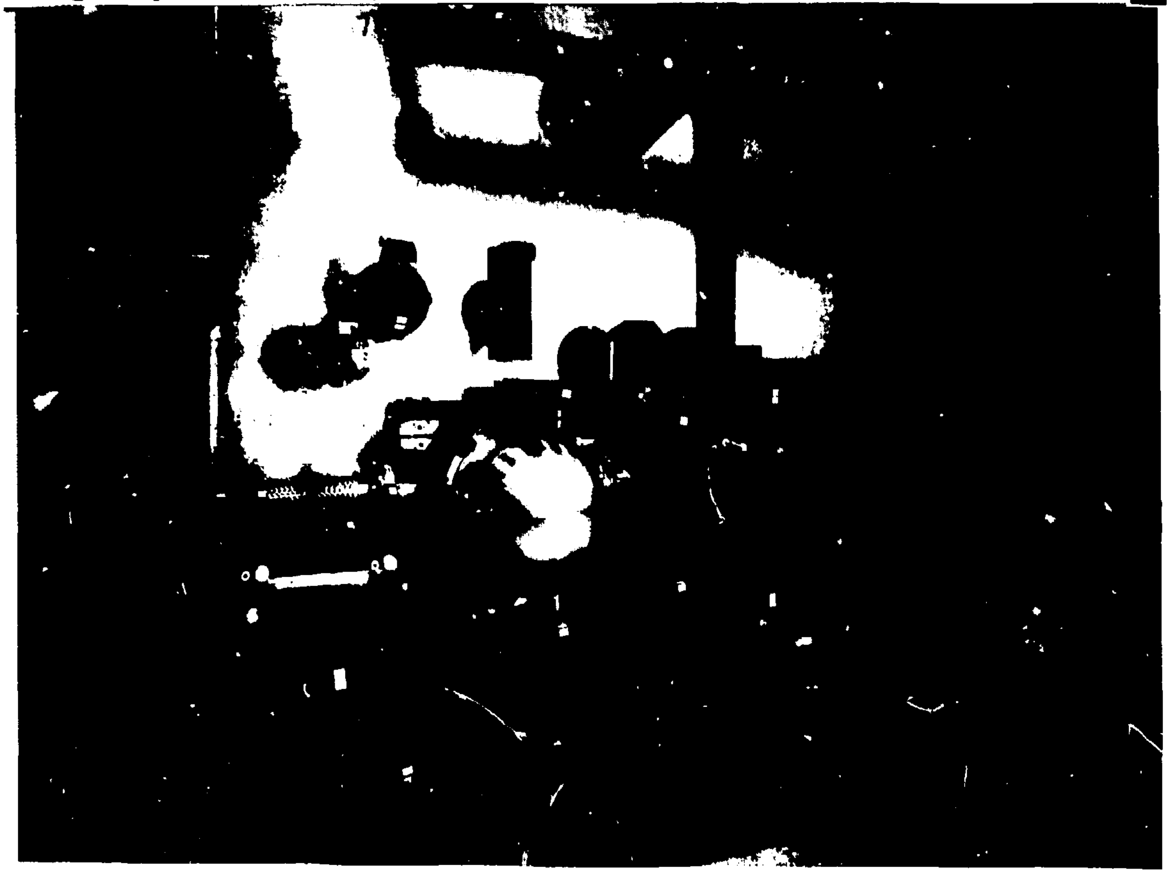

Fig. 40

SDF separator

Fig. 41

Half-scale separator facility

Fig. 42